MECHANOCHEMICAL MODELS FOR COLLECTIVE CELL MOTILITY

by

Sarita Koride

A dissertation submitted to The Johns Hopkins University in conformity with the requirements for the degree of Doctor of Philosophy.

Baltimore, Maryland

February, 2016

Abstract

At the tissue level, cells form a continuous sheet with no intercellular spaces. Dynamic behavior of these sheets is essential for tissue repair, organ formation in an embryo, and cancer metastasis. This dissertation explores mechanochemical models based on first principles to understand collective cell motility within epithelial layers. Specifically two situations are considered – morphogenesis in a Drosophila egg chamber, and dynamics of confluent monolayers on confined and unconfined geometries.

During tissue elongation from stage 9 to stage 10 in Drosophila oogenesis, the egg chamber increases in length by about 1.7 fold. During these stages, spontaneous oscillations in the contraction of cell basal surfaces develop in a subset of follicle cells. This patterned activity is required for elongation of the egg chamber. However, the mechanisms generating these spatiotemporal patterns have been unclear. Here, we use a combination of quantitative modeling and experimental perturbation to show that mechanochemical interactions are sufficient to generate oscillations of myosin contractile activity in the observed spatiotemporal pattern. We propose that follicle cells in the epithelial layer contract against pressure in the expanding egg chamber.

ABSTRACT

As tension in the epithelial layer increases, Rho-kinase signaling activates myosin assembly and contraction. The activation process is cooperative, leading to a limit cycle in the myosin dynamics. Our model produces asynchronous oscillations in follicle cell area and myosin content, consistent with experimental observations. In addition, we test the prediction that removal of the basal lamina will increase the average oscillation period. All together, the model demonstrates that in principle, mechanochemical interactions are sufficient to drive patterning and morphogenesis, independent of patterned gene expression.

To model confluent monolayers on confined or unconfined geometries, we use a vertex model, where each cell is modeled as a polygon and motion of its vertices is governed by forces arising from cell-cell friction, cell substrate friction, cell elasticity, pressure, surface tension, and intrinsic contractile forces due to molecular motors. Since contractility is an active process, we have a biochemical signaling network, which is a negative feedback loop, regulating the magnitude of contractile force based on cell perimeter change. Collective cell motility modeled this way, has the same density dependent average velocity and myosin levels as in experiments. Moreover, on ring substrates, cells show counter rotation at the inner and outer boundary at short time scales (a few hours) and vortex formation as seen in experiments. Methods to incorporate an active protrusive force, based on Rac signaling pathway and cell death and cell division are underway. All in all, this model is a promising method to understand collective cell motility in a variety of conditions.

ABSTRACT

Primary Reader: Dr. Andrew Ewald

Secondary Reader: Dr. Konstantinos Konstantinopoulous

Acknowledgments

It goes without saying that this thesis would not have been possible if not for the amazing help, support, and guidance I received from many people. First, I would like to thank - Dr. S. S. Ghosh, Dr. Biplab Bose, Dr. Rajaram Swaminathan, Dr. Ramesh Aiyyagari, and Dr. Alessandro Senes - professors from my undergraduate years who encouraged me to pursue research.

My deepest thanks to Dr. Sean Sun for his invaluable mentorship. He welcomed me into his lab in my second year in the program and guided me to do good research through the years with utmost patience. Alternating between the roles of a critic and a supporter, he pushed me to think clearly about a problem. I thank Dr. Denis Wirtz for giving me the opportunity to work in his lab, when I first joined the ChemBE department at Hopkins. Though I signed in to do experiments in his lab, I am thankful to him for giving me the freedom to work on purely modeling projects.

I sincerely thank my annual review committee members in the past few years - Dr. Zachary Gagnon and Dr. Rebecca Schulman for their comments and suggestions

on my work. I would like to thank my GBO committee members - Dr. Andrew Ewald, Dr. Yun Chen, Dr. Elizabeth Chen, Dr. Konstantinos Konstantinopoulos for taking the time to be on my committee.

Being co-advised, I was able to get immense support and help from all of Dr. Sun and Dr. Wirtz's lab members. I would like to thank Allison Chambliss and Wei-Chiang Chen for mentoring me in one of my first experimental research projects. I thank Angela Jimenez, Jude Phillip, Anjil Giri and Donghwee Kim of Wirtz Lab working along side whom was a great experience. I thank Osman Yogurtcu for helping me out from the time I first joined Dr. Sun's lab; for all the tea chats we had related to research and otherwise. I deeply appreciate the useful discussions I had and guidance I received from Ganhui Lan in my follicle cell oscillations project. I am grateful to senior members of the lab - Jin Seob Kim, Bo Li and Evgeny Stukalin from whom I learnt a great deal. I thank Yizeng Li for always being available to chat about anything at all. I thank Flori Yellen, Nash Rochman, Fangwei Si, Jim Tao, Santosh Paidi, Ted Grunberg and Dhruv Vig for making the lab a wonderful and entertaining place.

I thank all of ChemBE and MechE's department staff for being incredibly helpful with administrative stuff. I especially thank Ashanti Edwards, Rosana Medina, Caroline Qualls, Tracy Smith, Mike Bernard, Kevin and Cynthia.

I thank all the great friends I made here over the years - Saamrat Kasina, Srinivas Aripirala, Venkat Prava, Abdul Majeed, Tania Banerji, Siddharth Gupta,

ACKNOWLEDGMENTS

Lye Lin Lock, Alyssa Gross, Evi Lowman, Neha Dixit, Akanksha Bhargava, and Balaji Krishnamachari. Life would not have been fun without them.

Last but definitely not the least, I thank my wonderful family for their endless encouragement and support.

Dedication

To my family

Contents

List of Tables

List of Figures

Chapter 1

Introduction

Migration of cells (cell motility) is a phenomenon crucial to several fundamental biological processes such as wound healing,[1] where cells at the edge of the wound move to seal it; cancer metastasis,[3] where cells move from one tumor site to form another tumor; and embryogenesis,[2] where cells move together in an organized manner to sculpt an organ. Cell motility can be triggered and directed either by chemical cues such as gradients of chemokines or growth factors, or physical cues such as geometric confinement, boundaries or pressure due to growth. While single cell motility is relatively well understood,[34] how that translates to a group of cells (collective cell motility) is not fully understood yet.[5]

1.1 Mechanics of single cell motility

Single cell migration has long been studied in eukaryotic cells moving on substrates *in vitro* which mimic the extra cellular matrix (ECM) in the body. The traditional view of single cell motility in two dimensions has three major steps. After receiving a (chemical

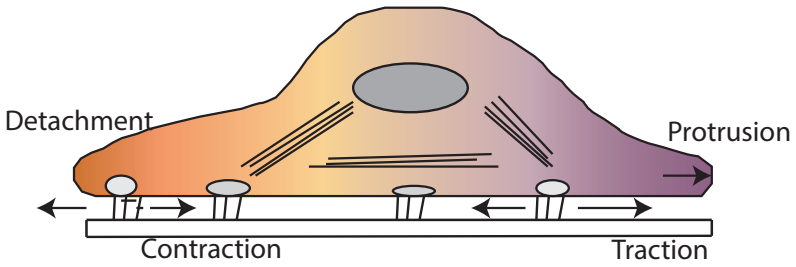

Figure 1.1: Illustration of single cell migration on a substrate. The three major components: protrusion at the cell front, disassembly at the back and translocation due to actomyosin contraction.

or physical) signal, the cell polarizes and extends a protrusion in that direction. This is followed by adhesion of the cell front to the substrate through focal adhesions which are macromolecular protein complexes that connect the cell to the substrate through integrins. At the rear of the cell, adhesions disassemble and the cell contracts to move forward as a whole (Fig. 1.1).

Mechanics plays a role in each of the above mentioned steps. Protrusion at the cell front through polymerization involves the actin filaments pushing against the cell membrane generating forces on the order of nanonewtons per micron.[6] Adhesions are the primary mechanotransducers of the cell. They relay information from the extra cellular environment to the cell about the ECM's stiffness or other mechanical properties which are then translated into biochemical signals interpretable by the cell.[7] The assembly and disassembly of these adhesions is one of the factors that determines the velocity of the cell. The actomyosin cortex of the cell then generates a contractile force to help the cell move forward.[8,9]

1.2 Mechanics of collective cell motility

Cells are viscoelastic materials having properties of both elastic solids and viscous fluids. Changes in mechanical properties of cells often correlate with pathological conditions.[12] For example, cell stiffness has been identified as a potential indicator of cancer metastasis.[11,13,14] These viscoelastic properties of cells can be quantified using techniques such as particle tracking microrheology, AFM techniques and magnetocytometry[10,15] .

At the tissue level, in addition to the forces mentioned in section 1.1, adhesions between cells through adherens junctions[16] also play a role in determining the emergent tissue dynamics. For example, studies have shown that adhesion strength could be a major factor in determining tissue fate during embryo formation.[17] Cells can also transmit force information through these contacts by pulling or pushing on each other. Cell sorting, another phenomenon during embryogenesis has been shown experimentally and through computational simulations to be dependent on cell-cell adhesions.[18]

Cells at the borders or cells in between a sheet could be extending protrusions[19,20] to move the sheet forward. Forces related to these protrusions could play an important role in guiding the movement of cells in a sheet.[21,22] However, the mechanics of protrusions in a sheet are not completely understood.

The elasticity of the substrate and the forces generated[23] can determine cell fate. Proliferation, migration velocity, and polarization are all shown to be dependent on cell's interaction with the substrate.[29–32] Interactions of the cell with the substrate through adhesions generate traction forces. Traction force microscopy or multiple-particle tracking microscopy with cells on flexible substrates are some of the methods used to map these

forces for a single cell or a sheet.[24–27]

1.3 Coupling of mechanics and signaling pathways

Force transmitted from the external micro environment of the cell, due to other cells pulling or pushing on it or due to traction force with the substrate, could lead to several biochemical changes in the cell.[28] Activation, deactivation, and localization of proteins which lead to polarization and eventual migration of the cell are shown to be dependent in some form with the external environment. One such family of proteins essential for cell migration are RhoGTPases.[33,34] The Rho family of GTPases are signaling G proteins belonging to the Ras family. RhoA, Rac and CdC 42 are the most important GTPases studied for their roles in cell motility and cytokinesis.[35] They switch between an inactive GDP form to an active GTP form upon receiving activation signals. They are also known for their role in several signal transduction pathways including actin cytoskeleton regulation, cell polarity and transcription factor activation.[36] Duct initiation in mammary epithelial morphogenesis,[22] Bordercell migration using photoactivatable Rac[21] are examples showing the importance of RhoGTPases in collective cell migration. Activation of these GTPases on application of external forces has been studied recently. On application of mechanical stresses through magnetic beads, Rac activation in the cell has been shown to be rapid and direct.[37] Activation of Rho in response to force and cyclic strain has also been shown in cardiac fibroblasts.[38] In light of these reports indicating the interdependence of mechanical signals and biochemical pathways, it becomes interesting and important to couple RhoGTPase activity to cell mechanics to understand the interplay between the two in the context

of cell motility.

1.4 Thesis Overview

This thesis aims to highlight the importance of understanding collective cell motility in the context of organogenesis and cancer metastasis through a modeling approach coupled with experimental results. Chapter 2 discusses the role of mechanics in the developmental process of Drosophila oogenesis. Incorporating Rho-ROCK-Myosin signaling in the form of a negative feedback loop into a mechanical model of the egg chamber during oogenesis results in basal cell surface oscillations in follicle cells, which have been observed experimentally. We discuss the roles of growth pressure and basal lamina in determining the periodicity of these oscillations. Chapter 3 explores the use of vertex models modeling cells as polygons with vertices - in understanding the effects of cell density and confinement on collective cell motion. Chapter 4 compares different stochastic simulation methods in mechanobiology.

Chapter 2

Role of mechanics in tissue development during Drosophila oogenesis

2.1 Introduction

The Drosophila ovary is composed of strings of developing egg chambers of increasing size and maturity (Fig. 2.1A a-d). Each egg chamber contains 16 germ cells surrounded by a monolayer of epithelial follicle cells. Egg chambers increase in volume over time while also becoming elongated. Follicle cell shape oscillations begin during stage 9 of development in a subset of cells near the center and correlate with increasing basal myosin content due to activation of Rho GTPase and Rho associated protein kinase, ROCK.[39] The maximal level of myosin activity and the number of cells undergoing oscillations increases

during stage 9 until most of the epithelium shows high myosin activity at stage 10 (Fig. 2.1A b-d). These observed oscillations in the basal surface area of follicle cells restrict the egg chamber width, and thus promote tissue elongation and morphogenesis. Autonomous periodic oscillations have been explored in other areas in biology.[40–42] Here we propose a mechanochemical model of cell contractility in the developing epithelium and investigate the spatial and temporal patterns in these oscillations using a combination of experiments and modeling. The model couples contractile forces generated by cells with mechanical tension from the external environment, including both the underlying germline cells and the overlying basal lamina. The model predicts that a cell can adjust its contractile force in response to external forces, and in some parameter regimes, the interplay of external tension and cell contractility leads to oscillations. Our model is based on the hypothesis that pressure on cells in the epithelium exerted by the growing germline cells induces the activation of the Rho-ROCK pathway,[38,43,44] which leads to a negative feedback in the form of myosin contractility. We model a section of the egg chamber as circular arrays of cells connected to each other in a staggered fashion (Fig. 2.1C-E). Cells are coupled mechanically to each other as well as to the basal lamina through mechanical springs in the circumferential and radial direction and angular springs in the axial direction. Forces developed by follicle cells are also under biochemical regulation. We investigate the interplay of biochemical signaling and mechanical forces during follicle cell length oscillations. The model predicts that the internal pressure of the egg chamber influences contractility of follicle cells. During egg chamber growth, increasing chamber pressure increases stress fiber formation and myosin contractility. Because cells are also mechanically coupled to each

other, oscillations in any single cell are also coupled to oscillations in neighboring cells. Depending on parameters, oscillations could in principle become synchronized. However, since only asynchronous oscillations are observed experimentally, the model suggests the ranges of pressure and contractile forces that are consistent with these observations. The model predicts that the basal lamina serves a mechanical role in the egg chamber development and affects both the size of the egg chamber and the periodicity of follicle cell oscillations. Without the basal lamina, the oscillation period should become longer. We tested these predictions by removing the basal lamina using collagenase, and observed an increase in the average oscillation period. We also use the model to examine mutants where some of the follicle cells do not exert contractile force. This simulated mosaic epithelium also exhibits oscillations with properties consistent with experimental observations. Taken together, the model identifies important mechanochemical variables within the developing egg chamber and presents a quantitative understanding of active forces within the epithelial layer. The model also shows that the interplay between mechanical forces and biochemical signaling pathways is sufficient in principle to explain the spatial and temporal patterning of myosin oscillations independent of gene expression, suggesting a novel patterning mechanism during tissue morphogenesis.

2.2 Model

Experiments show that basal surface area oscillations in the follicle cells during stages 9-10 of egg chamber development are mostly in the dorsal-ventral axis direction.[39] Based on this, a cross section of the egg chamber with unit cell width and radius r, is

represented by a circular array of cells. A change in the basal cell surface area is modeled as a change in the cell length in the dorsal-ventral (D-V) direction. The length of each cell is described by angular positions of the cell edges, i.e., the length of the i-th cell is $r(\theta_{i+1} - \theta_i)$. We also assume that the passive cell behaves elastically with stiffness k_c. Experiments show that D-V oscillations are driven by periodic assembly and activation of myosin on actin stress fibers at the basal surface. Therefore, we model this actomyosin contraction in the i-th cell as an active force, F_i, contracting the cell length (see Fig. 2.1F). Interaction between two cell layers in the A-P direction are modeled as elastic. When a cell contracts, it exerts mechanical forces on its neighbors. We model this passive mechanical interaction between cells using angular springs (Fig. 2.1C).

In the egg chamber, follicle cells are physically adhered to the basal lamina. Therefore, when the cells contract in the D-V direction, they exert an inward radial pulling force on the membrane. We neglect the relative motion between the follicular epithelium and the basal lamina, and model the deformation of the basal lamina using radial springs with stiffness k. Finally, it is known that the egg chamber is also under expansive internal pressure, probably from germline growth and the mechanics of nurse cells and oocyte within the epithelium. We include this pressure in the model using the parameter P.

Experiments show that increased contraction is correlated with increased myosin accumulation within stress fibers at the basal surface. Therefore, the biochemistry of myosin activity likely regulates active contraction of the follicle cells. In addition, the period of cell contraction is on the order of several minutes. This timescale is two orders of magnitude longer than the time scale of myosin binding and unbinding to actin, which occurs within

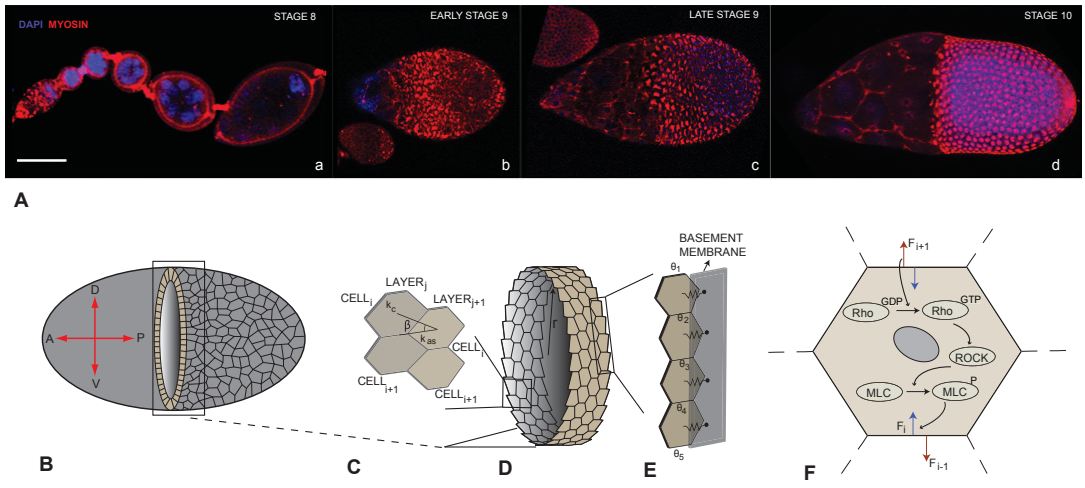

Figure 2.1: (A) (a-d) Egg chambers labeled with DAPI and myosin-mcherry (surface view) at stage 8 (a), early stage 9 (b), late stage 9 (c) and stage 10 (d). Maximum intensity projection of the z-stacks shows the early stage apical concentrated myosin and basal accumulation of myosin after stage 9. Scale bar = 50 μm. (B) Mechanical model. Cartoon of surface view of a Drosophila egg chamber showing the dorsal ventral (D-V) and anterior posterior (A-P) axis. Midsection of the egg chamber is zoomed in, in (D). Cells are modeled as springs of stiffness k_c in the D-V direction and are connected in the A-P direction through angular springs of stiffness k_{as} and preferred angle β as shown in (C). Connection to the basal lamina is shown in (E). Each cell is identified by the angular positions of its ends θ. (F) Biochemical model. Molecular pathway governing the activation of myosin contraction in response to tension. F_i (blue arrow) represents contractile force from the i-th cell and F_{i-1} and F_{i+1} (red arrows) represent forces on the i-th cell by neighboring cells.

seconds. Moreover, inhibition of Rho or ROCK prevents myosin assembly and contraction while constitutive activation of Rho causes constitutive assembly and locks myosin in the fully assembled and contractile state.[39] Therefore, mechanochemical aspects of Rho-ROCK signaling are probably key to understanding D-V oscillations. It is known that when a cell is under tension (here, mostly due to mechanical tension from internal pressure), Rho becomes activated within several minutes.[38] Rho activates ROCK, a protein kinase that further phosphorylates myosin light chain (MLC),[45,46] leading to myosin contraction. We

assume that the contractile force is directly proportional to the fraction of activated myosin. The modeled signaling pathway is shown in Fig. (2.1F).

2.2.1 Mechanical Model

For a cross section of unit cell width as in Fig. 2.1E, motions of the cell ends in the r and θ directions can be obtained from a mechanical energy formulation of the cell layer. This energy is a sum of the elastic energies - from follicle cells as well as the connectors to the basal lamina, the work done by the actomyosin contractile force and the work done by pressure P inside the egg chamber. The mechanical energy per length is then

$$E = \underbrace{\sum_{i=1}^{N} \frac{1}{2} k_c (r(\theta_{i+1} - \theta_i) - l_o)^2}_{\text{Cell length}} + \underbrace{\frac{1}{2} Nk(r_o - r)^2}_{\text{Basal lamina}} \\ \underbrace{- \sum_{i=1}^{N} F_i r(\theta_{i+1} - \theta_i)}_{\text{Contractile force}} - \underbrace{P\pi r^2}_{\text{Pressure-volume}} \tag{2.1}$$

where r is the radius of the circular cell array and is assumed to be the same for all the cells, l_o is the rest length of the cell, N is the number of cells in a cross section, Nk is the effective stiffness of the basal lamina, and r_o is the basal lamina preferred radius.

At the scale of the egg chamber, inertia is unimportant and forces are balanced by friction. Equations of motion for r and θ_i can be obtained from the mechanical energy by differentiation with respect to these variables and equating them to friction. The equations

are then

$$\begin{aligned}
\frac{dr}{dt} &= -\frac{1}{\gamma}\frac{\partial E}{\partial r} \\
&= -\frac{1}{\gamma}(k_c r \sum(\theta_{i+1}-\theta_i)^2 - 2\pi k_c l_o - \sum F_i(\theta_{i+1}-\theta_i) \\
&- 2P\pi r + Nk(r-r_o) \qquad (2.2) \\
\frac{d\theta_i}{dt} &= -\frac{1}{\eta}(\frac{1}{r^2}\frac{\partial E}{\partial \theta_i}) \\
&= -\frac{1}{\eta}(k_c(2\theta_i-\theta_{i-1}-\theta_{i+1}) + \frac{1}{r}(F_i - F_{i-1})) \qquad (2.3)
\end{aligned}$$

where η and γ represent the frictional coefficients in the θ and r. Thus, we propose that in the absence of cellular contractile forces, follicles cells are stretched by internal pressure, P. We propose that the cells generate contractile force that opposes the egg chamber pressure, and it is the biochemical control of the contractile stress that generates oscillations.

2.2.2 Biochemical Model

Models of Rho-ROCK signaling pathway have been studied before.[47,52] Here we propose a model where the activation of Rho and myosin are related to mechanical tension in the cell. Increased activation of Rho, ROCK and MLC in tissue cells in response to external tension has been observed.[38] We propose that this also occurs in follicle cells. The kinetics of Rho, ROCK and MLC activation in the i-th cell are modeled as

$$\frac{d\rho_i}{dt} = f_\rho(s_i)(1-\rho_i) - D_\rho \rho_i \qquad (2.4)$$

$$\frac{dR_i}{dt} = f_R(\rho_i)(1 - R_i) - D_R R_i \tag{2.5}$$

$$\frac{dm_i}{dt} = f_m(R_i)(1 - m_i) - D_m m_i \tag{2.6}$$

where ρ_i, R_i, m_i represent the fraction of activated Rho, ROCK and MLC respectively. s_i is the change in length of the i-th cell, $(r(\theta_{i+1} - \theta_i) - l_o)$ (the mechanical tension is then $k_c s_i$). Every rate equation has an activation and a deactivation part. The deactivation part is linear, which can represent any number of biochemical mechanisms such as hydrolysis of Rho^{GTP} to Rho^{GDP}, or constitutive phosphatase activity that inactivates ROCK. In the activation part, $f_\rho(s)$ represents the effect of the mechanical tension on the activation of Rho. Similarly $f_R(\rho)$ and $f_m(R)$ represent effect of Rho on ROCK and the effect of ROCK on MLC respectively. Mathematically, to obtain sustained oscillations, nonlinearity in the system is essential.[42] We incorporate nonlinearity in the form of a Hill function for the effect of tension on the activation of Rho, representing possible cooperativity in Rho activation:

$$f_\rho(s) = A_\rho h(s)(s^n/(K_s + s^n)), \tag{2.7}$$

$$f_R(\rho) = A_R \rho, \tag{2.8}$$

$$f_m(R) = A_m R \tag{2.9}$$

where h is a heaviside step function which is zero when s is negative and 1 when s is positive. This ensures that Rho gets activated upon cell stretching under tension. $A_\rho, A_{R,} A_m$ are the rates of activation and $D_\rho, D_{R,} D_m$ are the rates of deactivation. K_s is the half maximal response constant and n is the Hill coefficient for cooperativity.

Since the contractile force F originates from the activation of myosin light chain (MLC), we can assume that the force is linearly proportional to the fraction of activated MLC. The proportionality constant F_{max} represents the contractile force of a cell when the activated myosin fraction is 1, i.e, the maximum contractile force.

$$F_i(t) = -F_{max}.m_i(t) \tag{2.10}$$

F_{max} is related to the total amount of contractile myosin available for the basal stress fibers, whereas F_i is related to the amount of activated myosin generating contractile force within the stress fibers. Note that the proposed mechanical signaling model explains why stress fibers and contractile force are in the D-V direction in follicle cells. For an approximately cylindrical egg chamber, the mechanical tension from the internal pressure P is PR in the D-V direction and $PR/2$ in the A-P direction. Therefore, for the same internal pressure, Rho activation and stress-fiber formation would occur in the D-V direction first. The internal pressure and the shape of the egg chamber determines the direction of oscillation.

2D Epithelial Layer. In the egg chamber, follicle cells form the epithelial sheet, therefore cells are coupled in the D-V circumferential direction as well as in the A-P direction (Fig. 2.1D). We model A-P mechanical coupling using angular springs. Therefore the total

energy of the epithelial sheet is

$$\begin{aligned} E &= \sum_{j=1}^{n}\sum_{i=1}^{N_j}\frac{1}{2}k_c(r(\theta_{j,i+1}-\theta_{j,i})-l_o)^2 - F_{j,i}r(\theta_{j,i+1}-\theta_{j,i}) \\ &+ E_{bm} + E_{as} - ndP\pi r^2 \qquad (2.11) \\ E_{bl} &= \sum_{j}\frac{1}{2}N_j k(r_o-r)^2 \qquad (2.12) \\ E_{as} &= \sum_{j}\sum_{i=1}^{N_j}\frac{1}{2}k_{as}\left(\beta_{j,i}-\beta_o\right)^2, \qquad (2.13) \\ \beta_{j,i} &= \arctan\left[\frac{r((\theta_{j+1,i+1}-\theta_{j+1,i})-(\theta_{j,i+1}-\theta_{j,i}))}{d}\right] \qquad (2.14) \end{aligned}$$

where j labels the row in the A-P direction and i label the cell in the same row in the D-V direction; E_{bl} is the energy of the mechanical springs connecting cells to the basal lamina, n is the number of cell rows. E_{as} is the energy corresponding to the angular springs (of stiffness k_{as}) connecting different layers, N_j is the number of cells in the j-th row, β is the angle made by angular springs with the horizontal and d is the distance between rows, which would correspond to typical cell width (Fig. 1). β_o is the preferred angle between cells in adjacent rows.

In this model, we assume that the cell-cell connections between rows is fixed, i.e the interactions are not dynamic. In reality, the connections are made through cadherin bonds and there is a adhesion component as well as a shear/friction component. We have neglected the shear component because the differences in angular velocities between rows are small. Therefore relative sliding of cells in adjacent rows is negligible.

2.3 Methods

2.3.1 Mathematical model

Our model has four cross sections (circular arrays of cells) stitched together into a cylindrical sheet; each cross section having 30 cells, making it a total of 120 cells in the system. Each cell has 4 equations corresponding to four variables - angular position, activated rho, ROCK and MLC fractions. In addition, there is one equation for the radius of the egg chamber. We solve this set of 481 differential equations simultaneously using MATLAB's *ode*45 for a time period of about 5 hours. Periodic boundary conditions are used. The initial conditions are generated randomly with the following constraints. The rho, ROCK, MLC fractions are below 1 and the angular positions of cells (begin and end positions) are chosen such the sum of all the angular cell lengths equals 2π.

2.3.2 Data analysis from experiments

Fly Stocks

Following fly stocks were used in this work: UAS-GFP-Paxillin, Ubi::DE-Cadherin-GFP, sqh::sqh-mcherry (from Dr. Eric F. Wieschaus), Talin-EGFP (MiMiC fly from Dr. Hugo Bellen), Viking-GFP (from Dr. David Bilder). All stocks and crosses were maintained at room temperature. Female flies, 3-7 days post-eclosion, were used for the experiment.

Live imaging and chemical treatment

Live imaging of drosophila egg chamber was done as previously described.[39] Time-lapse-image was carried out on either Zeiss 710 NLO confocal microscope using 40X, N.A.

1.1 water immersion lens, or Olympus FV1200 confocal microscope with 40X, N.A. 1.25 oil immersion lens. Z-stacks with 2-3 slices (3uM in thickness) were taken to capture the entire basal myosin. The maximum intensity projected images were used for analysis. In chemical treatment experiment, egg chambers were first dissected in live imaging medium. Then the dissection medium was removed and replaced by medium containing Collagenase (1mg/ml, Sigma), Latrunculin A (100uM, Sigma), or Ionomycin (2.5uM, Invitrogen). Then egg chambers were either mounted immediately for live imaging or incubate in the medium for 1hr before quantification. 4% formaldehyde was used for fixative experiment. Alexa 569-conjugate phalloidin (1:300, invitrogen) was used for F-actin staining.

Image Analysis of Fly Movies

Live drosophila egg chamber movies, imaged at 60 second intervals for an hour during stage 10A, were analyzed to calculate oscillation period. Myosin intensity is calculated as follows. The myosin labelled images are first filtered using a Gaussian blur filter with a radius of 25 pixels in ImageJ. These images were then subtracted from the originals as background. After enhancing contrast, the images were segmented using a software *ilastik*.[60] Segmented images were manually checked for errors using photoshop and analyzed using MATLAB for myosin intensity and cell area measurements. The myosin intensity is normalized with respect to maximum value for each of the frames and plotted as a function of time in Fig. 2.2. Myosin intensity measurements were used to calculate oscillation period using autocorrelation as they were less noisy than the surface area data. Distances between peaks in the autocorrelation plot of myosin intensity gives the period distribution. A total of 87 cells in the control condition and 91 cells in the collagenase treated condition were

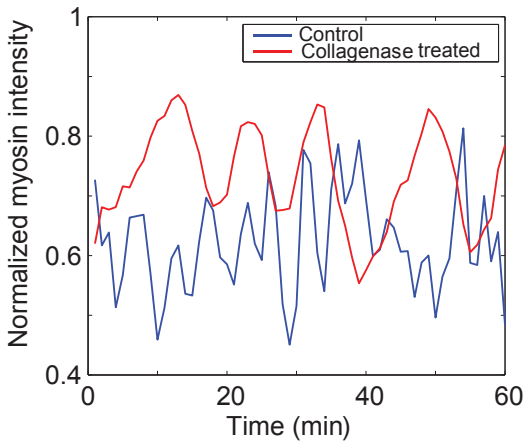

Figure 2.2: Raw data from experiments - Normalized myosin intensity plotted as a function of time in control and collagenase treated samples.

analyzed to calculate the period in each case.

2.3.3 Parameters

The list of parameters used is given in tables 2.1 and 2.2. The friction coefficients η and γ are set to be 100 nN.s/μm, from previous reports on embryo relaxation time obtained from laser ablation experiments.[64,65] The stiffness of each spring, k_c was set to 1 nN/μm per unit cell width to produce a relaxation time of 100 seconds.[65] In reality, cell stiffness could be a function of myosin content. The number of cells N, is estimated to be 30, from experimental evidence.[39] The rest length of the cell is assumed to be the average cell length from experimental data and is set to 6 μm.[39] Typical cell width, d is set to 5 μm. The stiffness of the angular springs k_{as} is set to 4 nN.μm.

The pressure inside the egg chamber, P , the stiffness of the basement membrane, k and maximum contractile force F_{max} are the variables in the system. Pressure is varied from 0.1 to 1 kPa, basement membrane stiffness is varied from 0.1 to 3 nN/μm per unit cell

width. The range for maximum contractile force is chosen such that forces experienced by the cell are within the nN range as seen in experiments.[25,45,66] It is varied from 10 to 60 nN per unit cell width.

The rates of activation and deactivation of Rho, ROCK and MLC are estimated to be as shown in Table 2.2. The intrinsic rate of Rho GTP hydrolysis is on the order of 0.022 per minute ($3x10^{-4}$ per sec) which can be stimulated to several fold by GAP proteins.[50] The Rho activation rate used in this paper [Table 2.2] could be thought of as a rate upon stimulation by tension. We assume other rates to be on the same order. To represent cooperativity, Hill coefficients are commonly chosen to be greater than 2,[40–42,47] we choose a value of 10 in our model.

2.4 Results

2.4.1 Single Cell Oscillates Under Mechanical Stretch

The simplest case is when a single follicle cell is under tension. This case is not possible to examine in experiments, but it is possible to explore using our model. Fig. 2.3 shows an example where an externally applied force stretches a single cell, and the force gradually increases with time (Fig. 2.3A). Our model predicts that the cell length will increase with increasing applied force (Fig. 2.3B), however, activated Rho will also increase with increasing applied force (Fig. 2.3C). The activated Rho catalyzes activation of myosin in the stress fibers and the cellular contractile force increases to oppose the applied force. Within a range of applied force, the Rho-ROCK signaling network exhibits oscillations. This oscillation is a limit cycle (Fig. 2.3E). The period of oscillation depends on the rate of

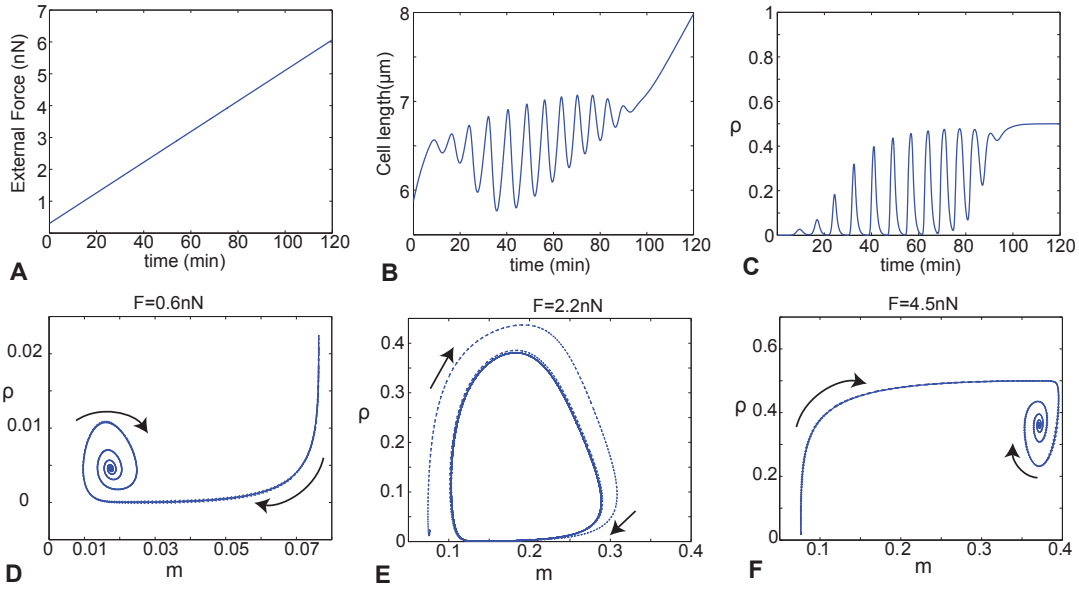

Figure 2.3: Behavior of single follicle cells. (A) As we apply an increasing external stretching force to a single follicle cell, we see that (B) the follicle cell length increases with increasing force. But as the force reaches a threshold the cell starts to oscillate. At large forces the oscillations disappear and the cell continue to stretch. (C) The amount of activated Rho increases with increasing force and there is an oscillation in the amount activated Rho. Rho reaches a maximum value at large force. (D,E,F) When the external force is held constant, 3 behaviors are seen. At low forces (D), the system settles to a steady level of activated Rho and MLC. At intermediate forces (E), the system exhibits an oscillatory limit cycle. At high forces (F), a steady state is again reached. Therefore, our model predicts a Hopf bifurcation with increasing external force.

Rho and ROCK activation. An analytic estimate of the oscillation period is shown in the Sec: 2.4.7.

2.4.2 Oscillations in cell D-V length and myosin content

When multiple follicle cells are mechanically connected in the epithelium, our model simulations show that the cells will oscillate along the D-V axis with an average period around 5-7min.[39] The oscillation amplitude ranges from 0.5-2 μm which also is what experiments observe.[39] Experiments show that oscillations in myosin intensity are correlated

to and precede oscillations in basal cell area in follicle cells.[39] In our model, normalized activated myosin also shows oscillations with periods similar to that of oscillations in cell length. Fig. 2.4A shows myosin and cell length oscillations on the same plot. Myosin activation precedes reduction in cell length as observed *in vivo*. We fit a cosine function to the computed oscillations and obtain the phase of oscillation for each cell. We find that this system at long times shows a uniform distribution of oscillatory phase (Fig. 2.4C). This suggests that the oscillations are asynchronous. If oscillations are synchronous, all cells would have a similar phase and the phase distribution would be more concentrated. We do find a synchronous phase in other parameter regimes (Fig. 2.4D,E). The observed oscillations are also independent of initial starting configurations of the model (Fig. 2.4B).

F_{max} and P are the important physical variables in this system. F_{max} is the maximum possible myosin contractile force, representing maximum activation of myosin. P is the internal egg chamber pressure. The pressure generates a tension of $T = Pr$ in the D-V direction of the epithelial layer. In response to this tension, cells activate myosin contraction to balance this tension. Note that there is also a tension in the A-P direction, but it is half of the tension in the D-V direction. Since increasing tension increases myosin activation, our model also predicts that the radius of the egg chamber will influence the observed myosin intensity. Indeed, we see that the combination of egg chamber pressure, geometry and epithelial tension is another mechanism of spatial pattern formation. Myosin activation responds nonlinearly to tension, and larger egg chamber radius will lead to a stronger activation. In an egg chamber with spatially varying radius but uniform pressure, myosin will become activated first in regions of larger radius.

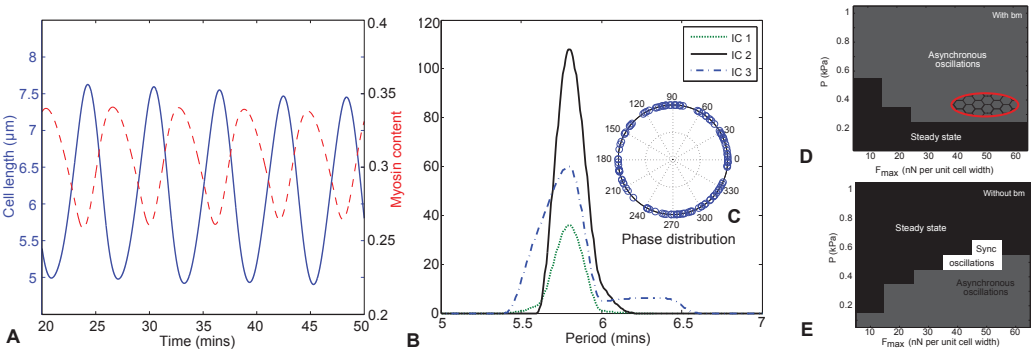

Figure 2.4: Follicle cell length and myosin oscillations. (A) Plot showing oscillations in cell length (blue) and in myosin content (red). Increase in myosin content corresponds to decrease in cell length. (B) Oscillation period distribution for different initial conditions (IC), showing that the range is in between 5 to 7 minutes and is independent of IC. (C) Phase distribution of oscillations in 120 cells showing that the oscillations are asynchronous. The phases are uniformly distributed around 2π. (D, E) Phase diagrams of oscillatory behavior with and without basal lamina. The system generally exhibits asynchronous oscillations or steady non-oscillatory behavior. There is a small synchronous oscillation regime without basal lamina (white), although this would require a high internal pressure. The red circle indicates, in our model, the region close to the physiological situation.

Computations show that frequency and amplitude of cell oscillations as well as the egg chamber radius and mean myosin intensity all depend on F_{max} and P. Oscillation period follows a decreasing trend with increase in F_{max}. For some parameter regimes, synchronized oscillations are also seen. We estimate that physiologically relevant parameters are close to $F_{max} = 50$nN and $P = 0.3$kPa.

We further investigated the effect of ROCK activation, and the radius of the egg chamber on the oscillation period. In experiments, it is possible to interfere with the activity of ROCK using Y-27632, a rock inhibitor. It was found that at inhibitor doses where oscillations persisted, the period largely remained unchanged. We model this experiment by varying ROCK activation rate, A_R in Eq. (2.8), and a similar behavior is observed. We still see oscillations and the oscillatory period depends non-montonically on A_R (Fig. 2.8). The

egg chamber radius does affect oscillation period. For smaller radii, higher contractile force is required to cause oscillations, whereas at larger radii, higher pressures induce oscillations (Fig. 2.11D).

2.4.3 The basal lamina plays a role in determining periodicity of follicle cell oscillations

In the egg chamber, the basal lamina is a highly crosslinked and complex structure, with collagens comprising about 50 percent of the protein.[48] Follicle cells adhere to the basal lamina via integrin-mediated adhesions that contain focal adhesion proteins such as talin and paxillin (Fig. 4A, 2.5). We examined the effect of the basal lamina on follicle cell oscillations by treating wild type (WT) cells with collagenase to partially remove the basal lamina surrounding the egg chamber (Fig. 2.6B). Fig. 2.6C shows the distribution of oscillation periods for control and collagenase treated samples. Upon collagenase treatment, some cells no longer exhibit oscillations. Other cells show an increased oscillation period. The mean period in the control condition is 5.6 minutes, which increases to 10.6 minutes. In addition, the egg chamber radius decreases by about 20 percent upon collagenase treatment (refer Fig. 2.6C inset).

In our model, we can examine the effects of the basal lamina by varying the stiffness of the mechanical spring connecting the epithelial layer to the basal lamina (k). We decreased k from 3 to 0 nN/μm per unit cell width in the simulations. In Fig. 2.6D, oscillation period is shown as a function of k. The general trend in the $P - F_{max}$ space is an increase in oscillation period as the stiffness decreases. In one of the cases, $P = 0.1$kPa, F_{max}= 60nN per unit cell width (red), the system starts from a steady state and goes to

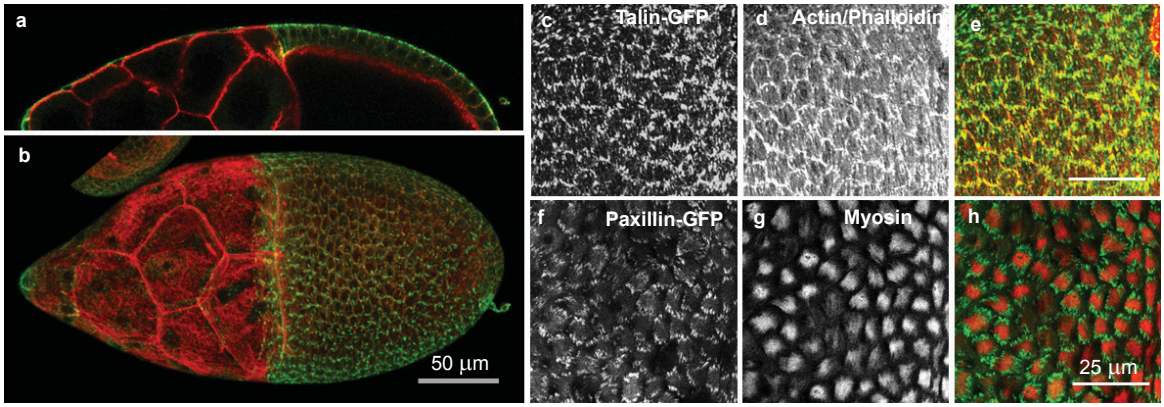

Figure 2.5: Coupling of basement membrane to basal myosin in follicle cells. Using GFP-tagged endogenous talin and UAS-Paxillin driven by heat shock Gal4, we observed an enrichment of focal complex at the end of the actomyosin fibers, which suggests that basal myosin is mechanically coupled to the basement membrane. (a) A sagittal plane through the center of a late stage 9 egg chamber expressing Talin-GFP and labeled with Phalloidin for actin. (b) Surface view. Scale bar is 50μm. (c-e). Micrographs of follicle cells labelled with Talin-GFP (c) and Phalloidin for actin (d). (f-h). Images of follicle cells labelled with Paxillin-GFP (f) and myosin-mcherry (g). Scale bar is 25μm.

an oscillatory phase with increasing period as stiffness decreases. In the other case shown (black), at $P = 0.3$kPa, $F_{max} = 50$ nN per unit cell width, the system shows a gradual increase in oscillation period as stiffness decreases.

2.4.4 Autonomy of cell oscillations

Experimentally, wild type cells surrounded by either constitutively relaxing cells (ROCK RNAi expressing cells) or with constitutively contracting cells (Rho V14 expressing cells) still oscillate with normal amplitude and period, indicating that these oscillations are cell autonomous.[39] We checked this in our simulations by surrounding wild type cells with those having no active Rho and ROCK (Fig. 2.6E,F). There seems to be no difference in period in neighboring and non neighboring wild type cells, as seen in experiments.[39]

2.4.5 Activation of myosin as a function of egg chamber width

Tension in the D-V direction of the egg chamber goes as internal pressure times the radius. As radius increases, increase in tension leads to activation of myosin. During stage 9 - 10, as egg chamber grows in size, we see increased myosin accumulation due to increase in egg chamber width.(Fig. 2.7)

2.4.6 Effect of drugs on oscillation period and egg chamber radius

Adding ionomycin, a drug that promotes contraction of actomyosin filaments, doubles the basal myosin intensity as well as reduces the egg chamber width by around 6%.[39] In our model, increasing the rate of activation of MLC has the same effect. (Fig. 2.8)

Treatment with various concentrations of Rock inhibitor Y-27632, decreased the myosin intensity but did not show huge variation in the oscillation period.[39] Decreasing the rate of activation of ROCK shows non monotonous behaviour of the oscillation period and decrease in activated myosin fraction, consistent with experiments.(Fig. 2.8)

2.4.7 Analytic estimate of oscillation period from a single cell model

For the single cell version of our model, the rate of change in cell length is given by

$$\frac{ds}{dt} = \frac{1}{\eta}(F_{ext} - k_c s - F_{max} m) \tag{2.15}$$

External force acting on the cell is denoted by F_{ext}. If F_{ext} is made a linearly increasing function of time, we see that the system goes into a stable limit cycle within a range of forces (Fig. 2). Here F_{ext} acts as the bifurcation parameter, as F_{ext} changes, the system

changes from a steady state to an oscillatory limit cycle as seen in Fig. 2.

The dependence of the oscillation period on parameters such as cell stiffness k_c, friction coefficient η and biochemical rates are studied using simulations. Since this full system of equations cannot be solved analytically, we compare period dependence from our simulations to the analytical solution for period obtained from a simpler single cell model at the bifurcation boundary.

A simple system to analytically solve is a two chemical component system, where we only have Rho and MLC. ROCK is assumed to be in steady state. The dependence of Rho on tension is simplified to be linear. The equations are as follows.

$$\frac{d\rho}{dt} = f_\rho(s)(1-\rho) - D_\rho\rho \tag{2.16}$$

$$\frac{dm}{dt} = f_m(\rho)(1-m) - D_m m \tag{2.17}$$

$$\frac{ds}{dt} = \frac{1}{\eta}(F_{ext} - k_c s - F_{max} m) \tag{2.18}$$

where

$$f_\rho(s) = A_\rho.h.s \tag{2.19}$$

$$f_m(\rho) = A_m.R \tag{2.20}$$

Performing linear stability analysis, the jacobian matrix for the above system of

equations at steady state is

$$J = \begin{vmatrix} -\widetilde{D}_\rho & 0 & \widetilde{A}_\rho \\ \widetilde{A}_m & -\widetilde{D}_m & 0 \\ 0 & -\widetilde{A}_s & -\widetilde{D}_s \end{vmatrix}$$

Parameter	Value	Units	Meaning	Reference
η	100	$nN.s/\mu m$	Friction coefficient in the tangential direction	[65]
γ	100	$nN.s/\mu m$	Friction coefficient in the radial direction	[65]
k_c	1	$nN/\mu m$	Stiffness of the spring representing cell length	[65]
N	30	-	Number of cells in a cross-section	[39]
l_0	6	μm	Rest length of each spring	[39]
d	5	μm	Average cell width	[39]
k_{as}	4	$nN.\mu m$	Stiffness of the connecting springs	–
k	0.1-3	$nN/\mu m$	Stiffness of basement membrane springs	–

Table 2.1: Mechanical parameters in the model

where

$$\widetilde{D}_\rho = \frac{D_\rho}{(1-\rho_{ss})} \tag{2.21}$$

$$\widetilde{A}_\rho = A_\rho(1-\rho_{ss}) \tag{2.22}$$

$$\widetilde{D}_m = \frac{D_m}{(1-m_{ss})} \tag{2.23}$$

$$\widetilde{A}_m = A_m(1-m_{ss}) \tag{2.24}$$

$$\widetilde{D}_s = \frac{k_c}{\eta} \tag{2.25}$$

$$\widetilde{A}_s = \frac{F_{max}}{\eta} \tag{2.26}$$

The eigen values are then the solutions of the equation

$$\lambda^3 + B\lambda^2 + C\lambda + D \tag{2.27}$$

where

$$B = \widetilde{D}_\rho + \widetilde{D}_m + \widetilde{D}_s \tag{2.28}$$

$$C = \widetilde{D}_\rho \widetilde{D}_m + \widetilde{D}_m \widetilde{D}_s + \widetilde{D}_\rho \widetilde{D}_s \tag{2.29}$$

$$D = \widetilde{A}_\rho \widetilde{A}_m \widetilde{A}_s + \widetilde{D}_\rho \widetilde{D}_m \widetilde{D}_s \tag{2.30}$$

Eq. (2.27) has either 1 or 3 negative roots given by Descartes rule of signs. For the three roots to have negative real parts, the Routh Hurwitz criterion[67] is $BC - D > 0$. Hence, the bifurcation boundary is given by

$$BC - D = 0 \tag{2.31}$$

Solving equations 2.16, 2.17, 2.18 along with 2.31, gives the external force at the boundary as well as the steady state values at that force. At this force, the system moves from a limit cycle to steady state.

At the bifurcation boundary, the analytic solution of the period is given by

$$Period = 2\pi\sqrt{\frac{B}{D}} \tag{2.32}$$

The bifurcation point in the full single cell model is found using simulations and the period is calculated at that external force. Unlike the simple model, this model has two bifurcation points, one at the onset of oscillations and one at its disappearance. To be consistent with the simple model, the bifurcation point where the limit cycle disappears is considered

for period calculation. The value of force at this point is different compared to the value obtained in the simple model. Plots showing comparison of the full model simulation results with the analytical estimate are in Figures 2.9 and 2.10. Though the magnitude of the period is different in both cases, as they are different systems, the trends of period dependence on various factors seems to be the same at the bifurcation boundary.

2.4.8 Parameter study in the multi-cellular model

In the multi-cellar model, oscillation period follows a decreasing trend with increase in F_{max}. On the other hand, the amplitude shows a consistent increase with increase in F_{max}. Egg chamber width shows a decreasing trend with increase in F_{max}, and as expected the mean myosin fraction shows an increase. The results shown in Fig. 2.11 A and C are all at $P = 0.4$kPa. Countour plots of oscillation period, amplitude, egg chamber radius and mean activated myosin fraction are plotted as a function of P and F_{max} in Fig. 2.12.

We further investigated the effect of the radius of cross section of eggchamber, the cell stiffness and angular spring stiffness between cell layers on the oscillation period. Angular spring constant did not play a role in affecting the period whereas a decrease in cell stiffness causes an increase in period (results shown at $P = 0.3$kPa, $F_{max} = 40$pN per unit cell width in Fig. 2.11B). At smaller eggchamber widths, higher contractile force (30 pN per unit cell width,0.2kPa) is required to cause oscillations, whereas at larger radii, higher pressures (10pN per unit cell width,1kPa) induce oscillations (Fig. 2.11D).

Parameter	Value	Units	Meaning
A_ρ	0.015	s^{-1}	Activation rate of rho
A_R	0.015	s^{-1}	Activation rate of ROCK
A_m	0.015	s^{-1}	Activation rate of MLC
D_ρ	0.015	s^{-1}	Deactivation rate of rho
D_R	0.004	s^{-1}	Deactivation rate of ROCK
D_m	0.015	s^{-1}	Deactivation rate of MLC
K_s	0.015	μm^n	Half maximum response constant
n	10	-	Hill coefficient

Table 2.2: Activation and deactivation rates of the Rho-Rock molecular pathway.

2.4.9 Other model predictions

If all cells exert the same contractile force and contractions are synchronized, then the forces exactly balance and there is no net torque on the egg chamber. However, because the oscillations are not synchronized, the net torque in the system is not exactly zero. Our simulations predict that if we incorporate shear motion between the basal lamina and the epithelial layer, the net torque will cause an overall rotation in the egg chamber against the basal lamina. This overall egg chamber rotation has been observed.[49] In addition, build up of stress fibers and oscillations of follicles cells start from the middle of the egg chamber where the radius is largest. As the chamber grows larger, the oscillatory region grows to encompass the whole epithelial layer. This is consistent with our tension-activated model because mechanical tension is directly proportional to chamber radius. For the same internal pressure, larger radius will activate Rho and myosin contraction first.

2.5 Discussion

We have introduced a mechanochemical model of follicle cell oscillation in the developing Drosophila egg chamber. The model describes the response of follicle cells to external forces, and how egg chamber mechanics can potentially influence biochemical signaling and contractile force generation. In particular, we suggest that the egg chamber is under internal pressure, and follicle cells together with the basal lamina, exert forces to balance the expansionary pressure. During egg chamber growth, the pressure gradually increases, leading to an increasing follicle cell contractile force. Eventually, the system undergoes a Hopf bifurcation with the egg chamber pressure as the critical parameter, and oscillations in contraction appear. We showed that the observed oscillations are not synchronized, and mechanical properties of the basal lamina can influence the frequency of oscillations.

In this paper we have focused on biochemical regulation of contraction by the Rho signaling pathway. This is because the time scale of oscillation is on the order of minutes, much longer than the time scale of myosin interacting with actin (seconds). Available estimates of Rho activation rates are consistent with the oscillation period.[50] However, the time scale of stress fiber formation in actin networks under force is also on the order of minutes.[51] Experiments have shown that Rho is necessary for the observed autonomous contraction and therefore we have focused on this pathway. We have also focused on a simplified 2D description of follicle cells mechanics. 3D mechanical models of epithelial cell morphology have been proposed.[53] Our model can be extended to the 3D regime by incorporating 3D cell shapes.

The proposed biochemical signaling model controlling cell contractility may have implication in other tissue cells. The model suggests that as external forces stretch the cell, the tension in the cell cortex or membrane increases. This triggers a cooperative activation of Rho GTPase and ROCK, leading to a cascade of phosphorylation events that eventually activates myosin light chain, stress-fiber formation and contractile force generation. This type of tension activated contractile force generation has been observed in fibroblasts.[38] Therefore, the basic framework of the model will likely apply to other cells and tissues.

The prevailing view of tissue development is that morphogens pattern cell fates and gene expression, which in turn determine patterns of differential mechanical properties that drive major morphogenetic events such as invagination during gastrulation or convergence and extension movements.[54–56] Patterns of active contractile forces are clearly an important element throughout morphogenesis.[57–59] Here we show that patterns of actomyosin contractility can in principle emerge from mechanochemical interactions alone, without an initiating event based on a pattern of gene expression or a morphogen signal. It will be interesting to determine if this is a widespread mechanism that shapes organs and tissues.

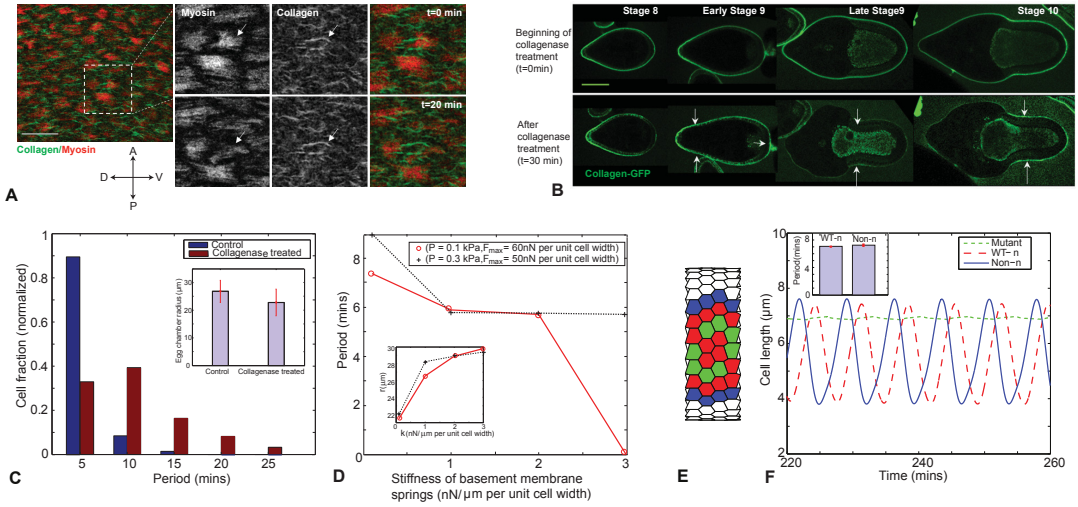

Figure 2.6: Effects of the basal lamina and mosaic analysis. (A) Images of basal lamina (labelled with collagen-GFP) and myosin (myosin-mcherry) in control conditions. The relative positions of collagen and myosin fibers remain unchanged, suggesting the basal lamina could be mechanically coupled to basal myosin. Scale bar, 20μm. (B) Egg chambers stained with collagen-GFP from stage 8 to stage 10 in control conditions, at the beginning of collagenase treatment ($t = 0$ min) and after collagenase treatment ($t = 30$ min). (C) Experimental measurements on follicle oscillations upon disruption of basal lamina.The distribution of oscillation periods became longer. The average egg chamber width became smaller (inset). (D) Modeling predictions of oscillation period as a function of stiffness of the basal lamina. Collagenase treatment reduces basal lamina stiffness and increases oscillation period for several values of P and F_{max}. The predicted egg chamber radius also becomes smaller as basal lamina stiffness is reduced, in agreement with experiments. (E) It is possible to abolish myosin contraction in some follicle cells using constitutively relaxing cells (ROCK RNAi expressing cells), these cells (green) do not oscillate. It is then possible to examine the interaction between the wild type cells (blue and red) with mutant cells (green). (F) Experiments and modeling show that there are no changes to oscillatory period in neighboring wild type cells (blue) or wild type cells directly neighboring mutant cells (green). Mutant cells however cease to oscillate. The oscillatory period is unchanged in neighboring vs. non-neighboring wild type cells (inset).

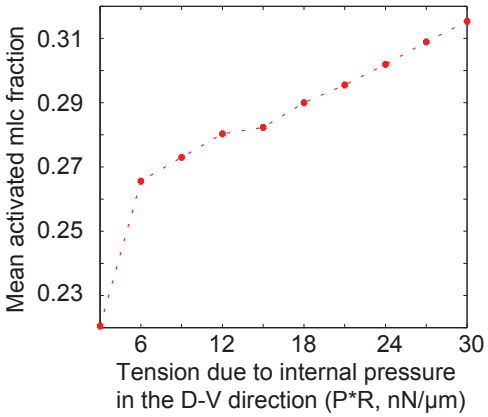

Figure 2.7: Activation of myosin as a function of egg chamber radius - Activated myosin fraction increases as the egg chamber tension in the D-V direction increases. Increase in radius at the same internal pressure P implies increased tension.

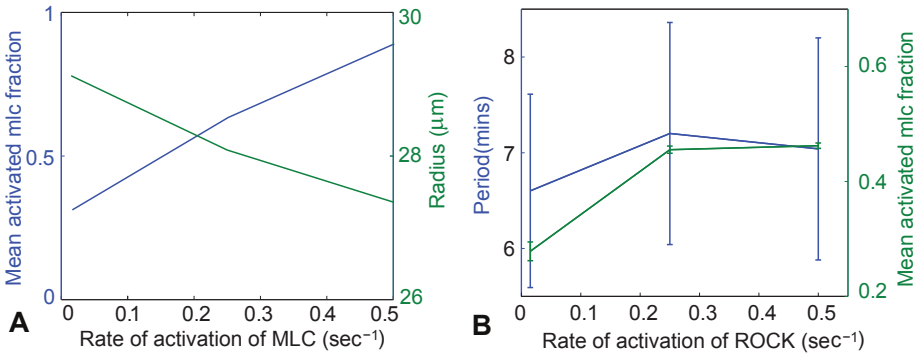

Figure 2.8: Pharmacological manipulation of egg chamber and its effects -Effect of adding ionomycin that increases the myosin intensity modeled as increasing the activation rate of MLC (A). Effect of ROCK inhibitor on oscillation period modeled as change in activation rate of ROCK(B). Parameters used are P = 0.1-0.3kPa and F_{max} = 20-30nN per unit cell width.

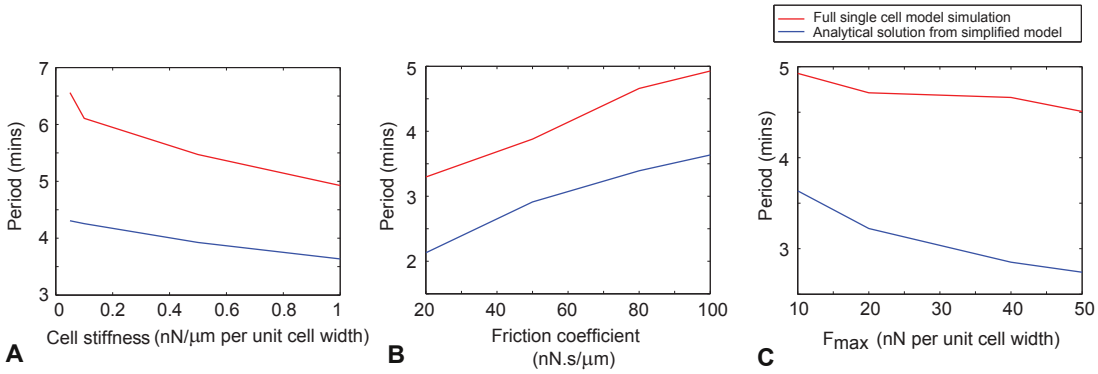

Figure 2.9: Single-cell model: Period dependence on mechanical parameters - The period at the bifurcation boundary decreases with increase in cell stiffness and maximum contractile force and increases with increase in the friction coefficient. Similar trends are observed in the full single cell model.

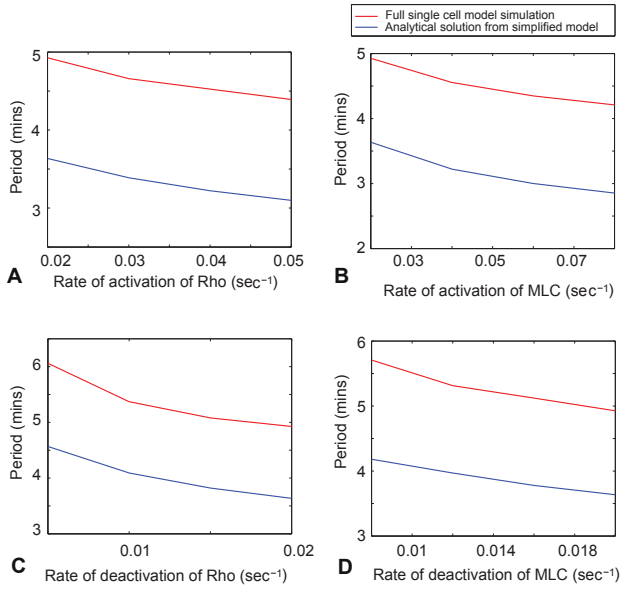

Figure 2.10: Single-cell model: Period dependence on biochemical rates - The period at the bifurcation boundary decreases with increase in rates of activation and deactivation of Rho and MLC. The full single cell model simulation follows the same trends as the analytical estimate for period from a simpler model. Value of F_{max} used in the single cell simulations is 10nN per unit cell width.

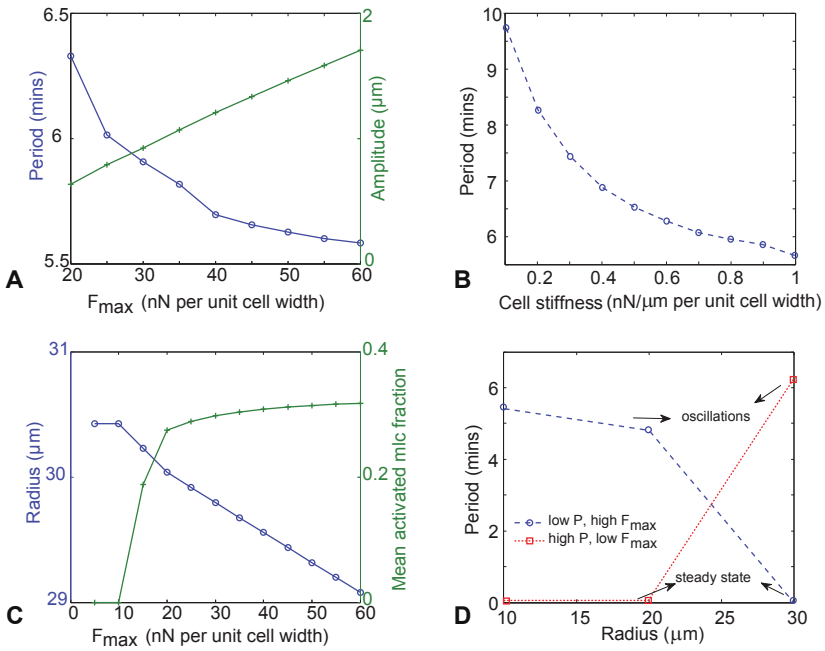

Figure 2.11: Multi-cell model: Parameter study - Decrease in oscillation period (blue) and increase in amplitude (green) with increase in maximum contractile force (A). Decrease in egg chamber cross-section radius (blue) and increase in mean myosin intensity (green) with increase in maximum contractile force (C). Oscillation period decreases with increase in cell stiffness (B). Change from oscillations to steady state with increase in egg-chamber radius at low pressure and high contracile force (blue). Change from steady state to oscillations with increase in egg-chamber radius at high pressure and low maximum contracile force (red) (D).

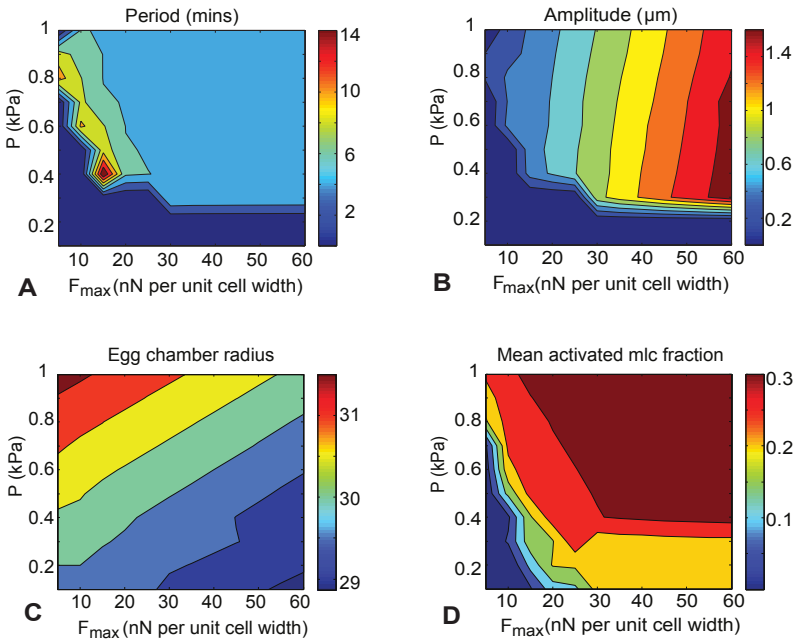

Figure 2.12: Multi-cellular model: Contour plots of oscillation period, amplitude, egg chamber radius and mean activated myosin fraction as a function of maximum contractile force and internal pressure. Slight decrease in period (in the range 5-7 minutes), as a function of Fmax at all P above 0.3kPa(A). Increase in amplitude as a function of Fmax (B). Decrease in egg chamber radius as Fmax increases (C). Increase in myosin intensity as Fmax increases (D).

Chapter 3

Vertex models for collective cell motility in confined and unconfined geometries

3.1 Introduction

Organized motion of epithelial cells as a group is crucial to developmental processes such as the basic organization of embryos and organ formation. Epithelia are tissues that form the surface for most organs in the body. They are broadly classified into simple mono layered and stratified (multi-layered) tissues. Depending on the shape of cells in the tissue, the mono layer simple epithelium can be further divided into squamous (flat cells), cuboidal (can take on any shape) and columnar (long, column like) epithelia. Irrespective of the type of epithelium, cells are connected to each other through three kinds of junctions

: tight junctions,[68] adherens junctions[69] and desmosomes.[70] Adherens/tight junctions are the primary force transducers between cells while the desmosomes act as barriers to flow of water and proteins between cells. Coordinated motion of cells in a sheet is facilitated by these junctions.

Complex shapes can be achieved during organ formation or embryogenesis due to coordinated cell movements and rearrangements. Examples include tissue folding and bending during gastrulation,[74,75] convergent extension[73] during tissue elongation, and neural tube formation.[72] Forces acting on cells play a key role in shaping a tissue.[76,77] These forces could be a result of intrinsic elasticity of a cell; from its tendency to resist stretch, or from cells pulling or pushing on each other through adherens junctions.[71] These forces could also result from a cells contractile ability coming from molecular motors.[78] Based on these forces, we can model the dynamics of the epithelial sheet.

Modeling epithelial cell dynamics can help us validate competing hypotheses and design further experiments to gain a better understanding of collective cell motility and organ formation. There are several models in place to understand sheet dynamics. These could be broadly classified into continuum and discrete models. Continuum models model the whole cell sheet as a two dimensional compressible fluid.[79] Discrete models consider cells as particles[83] and model their behavior based on forces acting on them. These discrete models can further be classified into lattice models,[80] cell-centered models[81,82] and vertex models.[84] Cell-centered models consider forces acting on the center of the cell and do not necessarily contain information about the shape of the cell. Vertex models more explicitly incorporate cell shape information, since each cell is modeled as a polygon representing the

cell membrane. Each cell vertex has an equation of motion which depends on its connections to other vertices and the properties of its neighbors. Vertex models have several advantages over cell-centered and lattice based models.Some of them are- (i) The cells are not limited to a particular shape. They can take on any shape based on the position of the vertices. (ii) Cell neighbor rearrangements can be very easily incorporated.

Vertex models were first used to understand dynamics of soap bubbles and foams.[85–87] These were later used to study epithelial dynamics, first by Honda and Eguchi.[88–90] Since then, many studies used similar models[91,92] for their ease of analysis to study cell packing and motion during morphogenetic events. Despite the prevalence of these models in studying epithelial dynamics, very few studies incorporate the role of cell signaling into these primarily mechanical models.

In this study, we bridge this gap. Recent studies have shown changes in activation of RhoGTPases in response to an external force.[37,38] In addition, pattern formation of RhoGTPases has been observed during wound healing.[93,94] RhoA is a principal mediator of cytoskeletal tension. Active Rho propagates downstream signals by binding to Rho associated kinase (ROCK). Phosphorylation of myosin light chain by ROCK leads to contractile force generation. To understand how active contractility which is dependent on GTPase signaling works hand in hand with cell shape changes and motion, we incorporated a Rho-Myosin signaling model within our vertex model. In the next sections, I describe the vertex model in detail (in Section 3.2) and then talk about two different aspects we studied using this model. Section 3.3.1 explores the effects of density on collective cell migration properties and the second section 3.3.2 explores the effect of confinement on motility. Finally,

we present a way in which the model could be improved to incorporate spatial dynamics of GTPases within each cell.

3.2 Model

Considering a two dimensional cross section of an epithelial layer, cells can be modeled as polygons, each identified by a set of vertices as shown in Fig. 3.1. The motion of the vertices determines the motion of the cell. A single vertex is shared by three cells and an edge is shared by two cells. A large system or a periodic system with N cells contains $2N$ vertices. A simple proof for it is as follows:

Let us say each cell has on average $\langle n \rangle$ vertices. Since each vertex is shared by three cells, the total number of vertices, $N_{vertex} = N\langle n \rangle/3$. Each edge is shared by two cells, so the total number of edges in the system, $N_{edge} = N\langle n \rangle/2$. The Euler relation requires that $N + N_{vertex} - N_{edge} = 1$, which gives

$$N\left(1 + \frac{\langle n \rangle}{3} - \frac{\langle n \rangle}{2}\right) = 1 \tag{3.1}$$

leading to

$$1 - \frac{\langle n \rangle}{6} = \frac{1}{N} \tag{3.2}$$

In the limit of a large system or a periodic system, $1/N$ approaches 0 and hence $\langle n \rangle = 6$. So we have $N_{vertex} = N\langle n \rangle/3 = 2N$. This tells us that the number of total vertices is known if we know how many cells the system contains. This property can be used to generate the initial distribution of vertices.

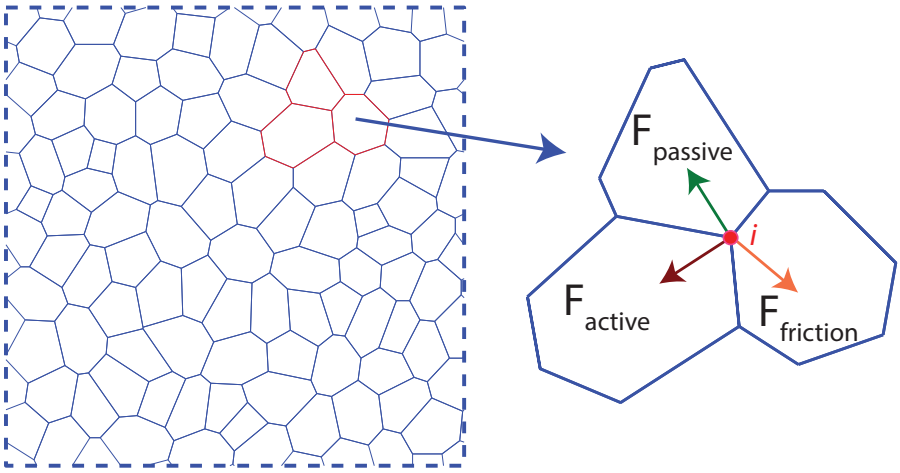

Figure 3.1: Description of vertex model. Cells in an epithelial sheet modeled as polygons. Each polygonal vertex is shared by three cells and each edge is shared by two. Motion of cells is determined by active, passive and friction forces acting on all the vertices that define the cell boundary.

3.2.1 Equation of motion of a cell vertex

Forces acting on a cell vertex can be classified into passive, active or frictional forces. At cellular length scales and time scales, inertia is negligible. Hence, a force balance can be implemented and an equation of motion can be written as shown below for each cell vertex (i).

$$\underbrace{\eta_s \frac{dr_i}{dt}}_{\text{cell- substrate friction}} + \underbrace{F_{fci}}_{\text{cell-cell friction}} = \underbrace{F_{pi}}_{\text{passive force}} + \underbrace{F_{ai}}_{\text{active force}} \tag{3.3}$$

$F_{csi} = \eta_s v_i$ is the friction between cell and substrate (viscous drag), η_s is the frictional coefficient, $v_i = \dfrac{dr_i}{dt}$ is the velocity of vertex i and r_i is its position. F_{fci} is the friction between cells, F_{pi} is the passive force arising from cell deformation and cell-cell adhesion. F_{ai} denotes the active force arising from cell contractility and polarization dynamics.

3.2.2 Passive force

Eukaryotic cells are mechanically rigid due to cytoskeletal filaments such as actin, microtubules, and intermediate filaments. Cells also control their volume by controlling their water content.[95] In addition, adhesion between cells in a sheet e.g. due to cadherin bonds results in forces that contribute to cell shape. Such passive forces can be calculated from an energy formulation (U_p) of the form

$$U_p = \sum_{J=1}^{N} \frac{K}{2}(A_J - A_0)^2 + \sum_{i,j} \Lambda l_{ij} \tag{3.4}$$

$$F_{pi} = -\frac{\partial U_p}{\partial r_i} \tag{3.5}$$

Here K is the area elastic modulus of the cell that describes resistance of cells to area changes, A_J is area of cell J, A_0 is the preferred cell area which could be a characteristic area dependent on the cell type, Λ is the adhesion energy per unit length and l_{ij} is the edge length between vertex i and j.

3.2.3 Active force

In addition to passive mechanics, cells also generate active forces. These could be from the intrinsic contractility of a cell due to molecular motors or cell's protrusions in the polarization direction. In this model, we consider three kinds of active forces - contractile force, persistent force and a random force due to polarization diffusion.

$$F_{ai} = \underbrace{F_{ci}}_{\textbf{Contractile force}} + \underbrace{F_{pi}}_{\textbf{Persistent force}} + \underbrace{F_{Ri}}_{\textbf{Random force}} \tag{3.6}$$

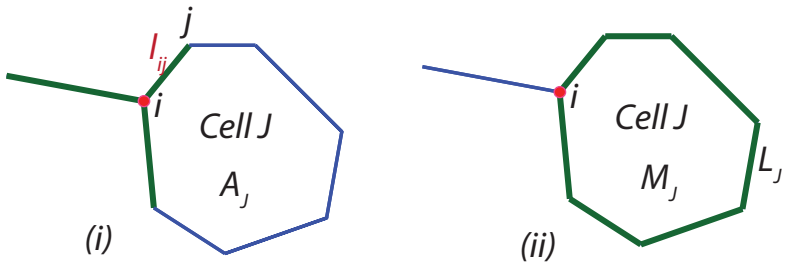

Figure 3.2: Forces acting on a vertex. (i) Passive force acting on a vertex due to area(A_J) elasticity and adhesion between cells. l_{ij} represents the cell edge connecting vertices i and j. (ii) Active force due to contractility acting on a vertex assumed to be dependent on the cell perimeter L_J and the amount of activated myosin in the cell M_J.

Contractile force

Phosphorylated myosin leads to contractile forces in the cell. Taking this into account, the contractile energy function (U_c) is assumed to be

$$U_c = \sum_{J=1}^{N} \frac{T_J}{2} L_J^2 \tag{3.7}$$

$$T_J = kM_J \tag{3.8}$$

where L_J is the perimeter of cell J and T_J is the contractility coefficient that is proportional to the amount of phosphorylated myosin, M_J in a cell which in turn is determined by the Rho-ROCK-Myosin signaling pathway described below.

Rho-ROCK-Myosin Signaling pathway

Studies suggest that when a cell is subject to an external stretch, activation of RhoGTPase increases.[38] This ultimately leads to phosphorylation of myosin which then tries to contract the cell,[46] resulting in a negative feedback loop. Although this pathway involves several other signaling molecules, we have used a simplified version of the pathway in this model. The simplified pathway involves only two components - Rho and Myosin but captures the underlying phenomenon. It is built into the model as a system of ordinary differential equations (ODEs). The level of activated RhoGTPase obeys the following ODE

$$\frac{d\rho_J}{dt} = A_\rho H(s_J)\frac{s_J^n}{K_s + s_J^n}(1 - \rho_J) - D_\rho \rho_J \tag{3.9}$$

where H is the Heaviside step function making sure ρ gets activated only in response to cell stretch, A_ρ is the maximum activation rate of ρ_J, $s_J = L_J - L_0$ is the stretch of the cell, L_0 being the preferred perimeter corresponding to the preferred area A_0, K_s is the half maximal response constant, n is the hill coefficient and D_ρ is the deactivation rate of ρ. The level of phosphorylated myosin follows a similar kinetic equation:

$$\frac{dM_J}{dt} = A_M \rho_J (1 - M_J) - D_M M_J \tag{3.10}$$

where A_M, D_M are activation and deactivation rates of myosin. Here we assume uniform spatial distribution of Rho or myosin within each cell. In reality, this is not true and there could be non uniform distribution of these molecules within the cell leading to polarization. In our model, this is modeled using a random force instead.

Persistent force

Cells migrate in a directed fashion over a characteristic time required to disassemble and reassemble cytoskeletal networks necessary for motility. Persistent force in our model comes from this ability to move in a certain direction persistently before making a turn. It is described phenomenologically as a term that depends on cell's past velocities and is as given below.

$$F_{pi} = \alpha \frac{\int_{-\infty}^{t} \exp(-\beta(t-t'))v_i(t')dt'}{|\int_{-\infty}^{t} \exp(-\beta(t-t'))v_i(t')dt'|} \tag{3.11}$$

where α is the strength of the persistent force, β is a constant that determines the decay rate of persistence, and $v_i = \dfrac{dr_i}{dt}$ is the velocity of the vertex i.

Random force

Random force due to polarization fluctuation is modeled as Gaussian white noise with zero mean and finite variance satisfying the following relations

$$< F_{Ri} >= 0 \tag{3.12}$$

$$< F_{Rq}(t)F_{Rs}(t) >= \sigma^2\delta(t)\delta_{qs} \tag{3.13}$$

where σ is the magnitude of variance characterizing magnitude of polarization fluctuation, and $\delta(t)$, δ_{qs} are Dirac's and Kronecker's δ-functions respectively.

3.2.4 Friction force

Cell-cell friction

Considering the part fluid like behavior of the epithelial sheet, friction between cells can be calculated from the in plane shear stress. This is computed using a finite volume approach. The cell-cell friction force experienced by a vertex is defined as the total shear force on the volume element[112] defined by a) the cell centers neighboring the vertex and b) the midpoints of neighboring edges as shown in Fig. reffig:frictionvolumeelement. Deviatoric stress, which is the total stress acting on a volume element minus the hydrostatic stress is as in Eq. 3.14. Frictional force is obtained by integrating this stress over the volume element.

$$\sigma_s = \eta_c(\nabla v + (\nabla v)^T - \frac{2}{3}\nabla \cdot vI) \tag{3.14}$$

$$F_{fc_i} = \oint \sigma_s \cdot n dS \tag{3.15}$$

where η_c is the cell - cell friction coefficient, ∇v is the velocity gradient within the volume element, S is the surface enclosing the volume element, and n is the outward directed normal to the volume. The fluid is approximately incompressible, so that $\nabla \cdot v = 0$, giving

$$\sigma_s = \eta_c(\nabla v + (\nabla v)^T) \tag{3.16}$$

Substituting this simplified form into the friction force equation, Eq.3.15 gives

$$F_{fci} = \eta_c \oint \nabla v \cdot n dS \tag{3.17}$$

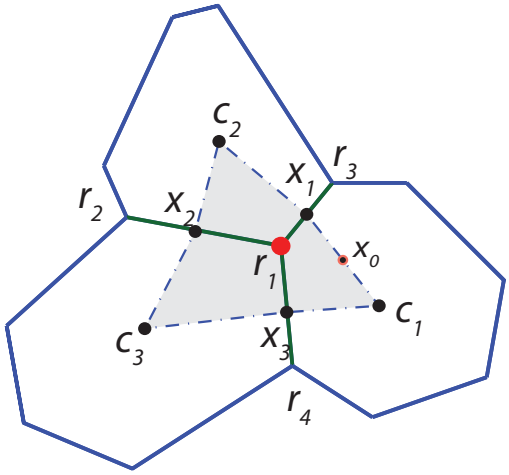

Figure 3.3: Finite volume element considered to calculate cell-cell friction. Assuming fluid like behavior of the epithelial sheet, frictional forces between cells in the sheet can be calculated from shear stress within the volume element.

Decomposing v and F_{fc} into x and y components, friction force can be written as

$$F_{fcx} = \eta_c \oint \nabla v_x \cdot n dS = \eta_c \oint (\frac{\partial v_x}{\partial x} n_x + \frac{\partial v_x}{\partial y} n_y) dS \tag{3.18}$$

$$F_{fcy} = \eta_c \oint \nabla v_y \cdot n dS = \eta_c \oint (\frac{\partial v_y}{\partial x} n_x + \frac{\partial v_y}{\partial y} n_y) dS \tag{3.19}$$

The velocity field can be computationally determined by a Taylor series expansion of the functions v_x and v_y about the midpoint of each edge of the volume element. Using the edge c_1x_1 with midpoint x_0 as an example, the expansion is:

$$v_x(x) \approx v_{x_0} + (x - x_0)\frac{\partial v_x}{\partial x}|_{x_0} + (y - y_0)\frac{\partial v_x}{\partial y}|_{x_0} \tag{3.20}$$

$$v_y(x) \approx v_{y_0} + (x - x_0)\frac{\partial v_y}{\partial x}|_{x_0} + (y - y_0)\frac{\partial v_y}{\partial y}|_{x_0} \tag{3.21}$$

where the nodes c_1, r_1 and r_3 are used to obtain

$$v_{x_0} = \frac{2v_x(c_1) + v_x(r_1) + v_x(r_3)}{4} \tag{3.22}$$

$$\frac{\partial v_x}{\partial x}|_{x_0} = \frac{r_{1y}[v_x(r_3) - v_x(c_1)] + r_{3y}[v_x(c_1) - v_x(r_1)] + c_{1y}[v_x(r_1) - v_x(r_3)]}{r_{1y}(r_{3x} - c_{1x}) + r_{3y}(c_{1x} - r_{1x}) + c_{1y}(r_{1x} - r_{3x})} \tag{3.23}$$

$$\frac{\partial v_x}{\partial y}|_{x_0} = \frac{r_{1x}[v_x(r_3) - v_x(c_1)] + r_{3x}[v_x(c_1) - v_x(r_1)] + c_{1x}[v_x(r_1) - v_x(r_3)]}{r_{1y}(r_{3x} - c_{1x}) + r_{3y}(c_{1x} - r_{1x}) + c_{1y}(r_{1x} - r_{3x})} \tag{3.24}$$

and

$$v_{y_0} = \frac{2v_y(c_1) + v_y(r_1) + v_y(r_3)}{4} \tag{3.25}$$

$$\frac{\partial v_y}{\partial x}|_{x_0} = \frac{r_{1y}[v_y(r_3) - v_y(c_1)] + r_{3y}[v_y(c_1) - v_y(r_1)] + c_{1y}[v_y(r_1) - v_y(r_3)]}{r_{1y}(r_{3x} - c_{1x}) + r_{3y}(c_{1x} - r_{1x}) + c_{1y}(r_{1x} - r_{3x})} \tag{3.26}$$

$$\frac{\partial v_y}{\partial y}|_{x_0} = \frac{r_{1x}[v_y(r_3) - v_y(c_1)] + r_{3x}[v_y(c_1) - v_y(r_1)] + c_{1x}[v_y(r_1) - v_y(r_3)]}{r_{1y}(r_{3x} - c_{1x}) + r_{3y}(c_{1x} - r_{1x}) + c_{1y}(r_{1x} - r_{3x})} \tag{3.27}$$

Analogous equations for the edges x_1c_2, c_2x_2, x_2c_3, c_3x_3 and x_3c_1 can be derived to compute the entire path integral and hence the friction force between cells.

Viscous drag

The coefficient of friction between the cell and the substrate as well as the media around it is assumed to be a constant η_s.

$$F_{csi} = \eta_s v_i \tag{3.28}$$

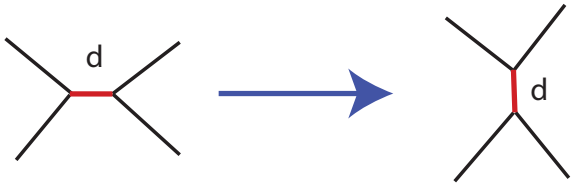

Figure 3.4: Topology changes. T1 transition, a neighbor exchange method to which allows changes in connectivity of vertices and allows cells to make and break bonds with neighbors

3.2.5 Topology changes

To faithfully represent collective cell behavior, we need to allow cells to break and make bonds. Topological changes i.e, changes in connectivity of vertices occur through T1 transitions. T1 transition is a neighbor exchange method which allows cells to make and break bonds with its neighbors. If the cell edge length goes below a certain threshold, T1 transition is allowed only if after the transition the two vertices of the edge move away from each other. The edge undergoing transition is rotated by 90^o around its midpoint as shown in Fig. 3.4. Additionally to maintain the integrity of the two dimensional system, restrictions are placed on the movements of vertices to ensure that edges do not cross or cells do not fold onto themselves.

3.2.6 Implementation

This model is implemented in both MATLAB and Fortran. All the parameters used in the model are listed in Table. 3.1. Parameters are rendered dimensionless using a length scale of $\sqrt{A_0}$, time scale of $\frac{\eta_s}{KA_0}$ and an energy scale of $KA_0^{3/2}$

Parameter	Value	Meaning
N	1000	Number of cells
η_s	1	Cell-substrate friction coefficient
K	5	Area elastic modulus
A_0	1	Preferred Area
Λ	0.5	Adhesion strength
k	2	Contractility coefficient
α	0.1	Strength of persistence
β	0.1	Decay rate of persistence
n	10	Hill coefficient
A_ρ	0.05	Activation rate of rho
A_m	0.01	Activation rate of MLC
D_ρ	0.05	Deactivation rate of rho
D_m	0.005	Deactivation rate of MLC
K_s	120	Half maximum response constant
n	2	Hill coefficient

Table 3.1: Model parameters

3.3 Results

3.3.1 Effect of density on motility

Motion of a single cell in a confluent layer depends on the local forces acting on it. These forces depend on its connectivity to its neighbors. The average number of neighbors a cell has can be important for determining the characteristics of collective motion. In other words, cell density or the number of cells per unit area of the sheet could be an important player in determining how organized motion is at the tissue level. Several experiments have shown the importance of density on collective cell motion[97–100] but exactly how it affects migration is not clearly understood.

To understand how cell density affects collective cell migration, we simulated cells in a square domain with periodic boundary conditions. We compared our simulation results

with experiments by tracking cells velocities and other properties at different densities. Varying densities are achieved experimentally either by plating a constant number of cells and measuring properties at progressively longer times or plating an increasing number of cells in the same area and measuring properties after 24 hours. Both cases yield the same results. To simulate this computationally, we changed density by fixing the number of cells but varying the simulation domain. Bigger box sizes simulate low density conditions and smaller box sizes represent high density conditions.

Mean cell speed decreases with increase in density

With increase in cell density, experiments show that there is a decrease in cell speed. To understand if cell-cell adhesion is the driver, we looked at cell speed at various densities in alpha-catenin knockdown cells in experiments. Alpha-catenin is a key component of cadherin-based junctions required for strong epithelial cell-cell adhesion.[101] A similar increasing trend in velocity was observed in the alpha-catenin knockdown cells as well. This tells us that other factors such as contractility might have an important role to play in determining mean speed at different densities. In wild type cells, simulations show a similar increasing trend in velocity as density decreased. In Fig. (3.5),simulated cell velocities (in grey) are shown as a function of radius. Here, cell radius is a proxy for density as it scales inversely with density.

Effect of lower cell-cell adhesion on cell speed

To simulate alpha-catenin knockdown we looked at two parameters in the model - line tension (Λ) and cell-cell friction coefficient (η). Increasing the line tension parameter in

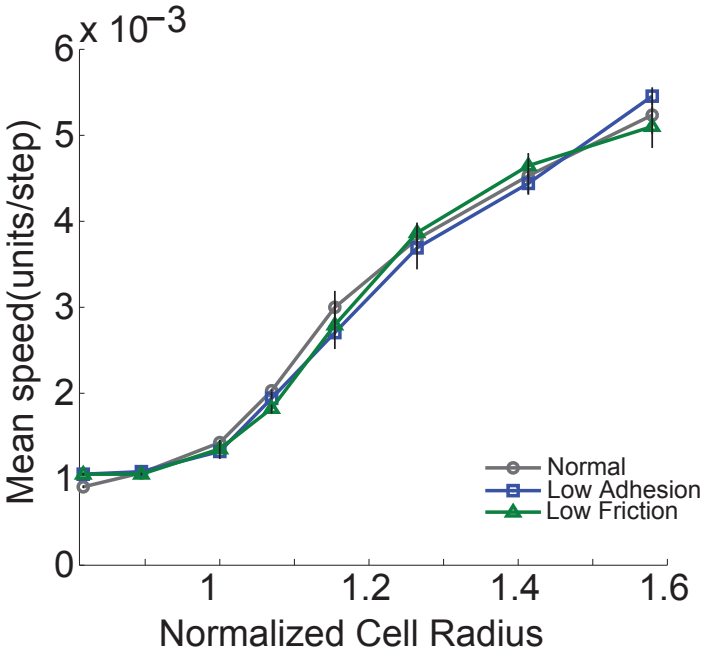

Figure 3.5: Cell speed as a function of average cell radius. As cell density increases, the average cell speed goes down. Even with low cell-cell adhesion and low cell-cell friction, the model shows similar decreasing trend in mean cell speed as density increases

the model is equivalent to decreased adhesion between cells. Another way of incorporating the effects of knocking down alpha catenin in the simulation is to decrease friction between cells. Both these parameters show the same cell speed dependence on density as the wild type as observed in experiments.

Mean myosin levels decrease with increase in density

In addition to looking at cell velocities which represent physical aspects of cell behavior at different densities, we could analyze the chemical state of the cells in terms of the mean myosin levels. We chose myosin levels as we know the intrinsic contractility of the cell depends on the amount of myosin present. The signaling component of the model

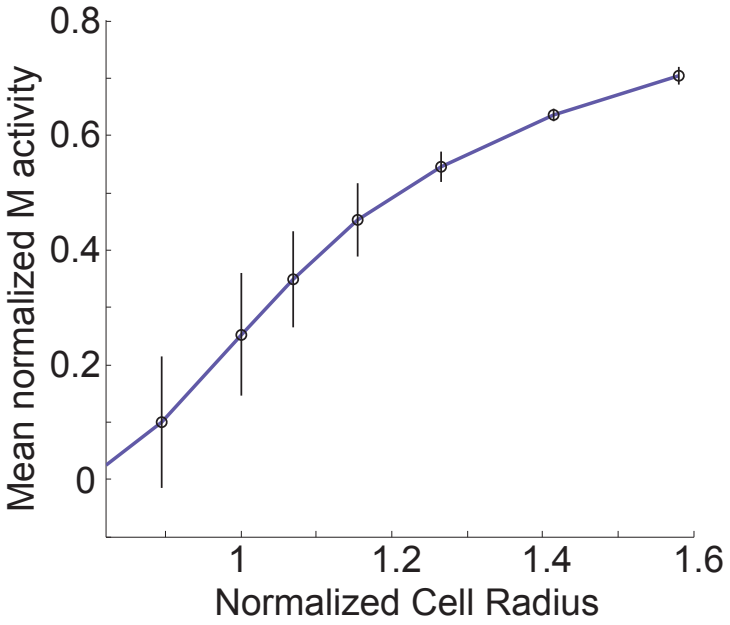

Figure 3.6: Mean myosin content as a function of average cell radius. As cell density increases, the average myosin content goes down.

gives us a way of looking at effects of density on the local myosin levels and hence the contractility of a cell. In experiments, we see that the myosin levels increase linearly with decrease in density or increase in effective cell radius. RhoA activation in the signaling component of our model depends on the change in perimeter experienced by the cell due to an external force. Since, increase in density implies a reduction in cell area/perimeter, myosin levels decrease in simulations as seen in experiments. This validates our hypothesis of stretch dependent myosin activation in a cell sheet.

3.3.2 Rotation of cells on a circular ring substrate

Cells migrating in physiological conditions experience various degrees of confinement either because of the extra cellular matrix acting as a boundary or by neighboring cells on multiple sides.[102] To understand cell motion in the presence of spatial constraints, several studies looked at cell behavior by confining single or multiple cells to micropatterned islands of different geometries. Huang et al[103] showed that when two or three cells are confined to mm scaled fibronectin islands of circular or square geometry, they exhibit spontaneous symmetry breaking and coherent rotation. This phenomenon has also been seen with large numbers of cells ($800 - 10,000$ cells per mm^2).[104] This type of rotation called as coherent angular motion has shown to be present during the morphogenesis of mammary gland acini and could be important for development.[105]

Recent experiments by Wan et al[106] have shown that cells on a ring substrate show counter rotation at the inner and outer boundaries. In addition, vortex formation in collective cell migration in narrow channels has also been reported.[107,108] However, we do not have a good understanding of how cell mechanics and biochemical signaling give rise to such behavior yet. Previously, a minimal cell centered model incorporating cell geometry and mechanics has been able to show rotation on circular substrates.[82] In this section, we use the vertex model to look at collective cell behaviors on geometries with two boundaries such as a circular ring.

Using our vertex model, we looked at cells confined to a ring shaped substrate as shown in Fig. 3.7. We looked at two different conditions - one where the contractility is independent of signaling and the other with a signaling pathway for active contractile

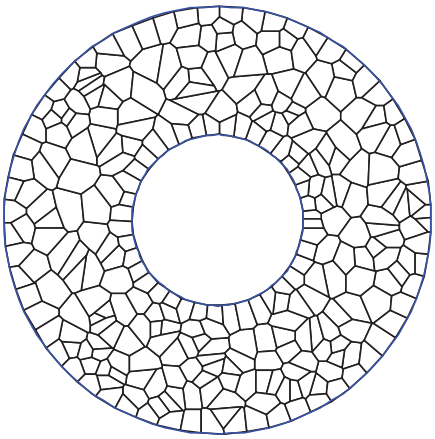

Figure 3.7: Vertex model in confined geometries. 300 cells modeled as polygons on a circular ring substrate. The ratio of inner to outer ring radius is 2 : 5. Blue circles represent the inner and outer boundaries beyond which the cells are not allowed to move.

force. In the first case the contractility coefficient is a constant and there is no signaling involved in the model. In the second case, we use the Rho-MLC pathway and make the contractility coefficient proportional to the amount of active myosin. In both these cases, two types of collective cell motions are seen on ring substrates - rotation or rotation with vortex formation (Fig. 3.8).

Vortex formation in the constant contractility coefficient model

In addition to coherent rotation that is also seen on circular substrates, cells on rings also show formation of vortices (Fig. 3.9 A). These vortices span the width of the ring and are dynamic in space and time. Since there is coherent rotation, on an average all the cells move with the same angular velocity. Hence, the mean circumferential velocity over all cells at long times, scales with the radius (Fig. 3.9 B). Plotting mean circumferential velocities at the inner and the outer boundaries as a function of time reflects the formation

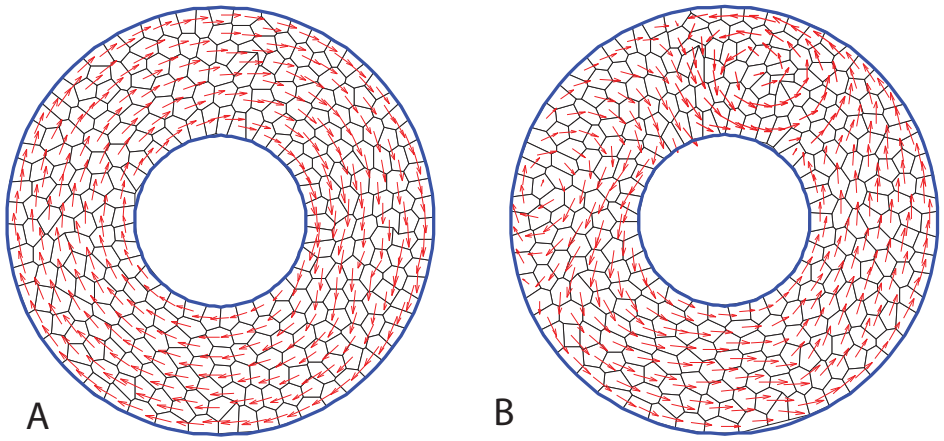

Figure 3.8: Types of collective motion seen in cells on a ring geometry. Cell velocity vectors show in in red. (A) Coherent rotation and (B) Rotation with vortices observed on ring substrates.

of vortices (Fig. 3.9 C). Here, the inner ring cells move in the opposite direction as compared to cells in the outer ring intermittantly. When there is no vortex formation during rotation, the circumferential velocities at the inner and outer rings move together as shown in Fig. 3.12. The ratio of the magnitudes of persistent force to random force determines whether or not cells exhibit coherent angular motion on ring substrates as seen in models of cells on circular substrates.[82] We also examined the parameter space of the strength of persistent force α and the memory decay rate β to see what causes the additional complexity of vortex formation during rotation. The range of α and β values that show rotation with vortices is shown in Fig. 3.9 D.

3.3.3 Model with signaling shows non uniform myosin distribution in cells on a ring

In the above mentioned version of the model, the contractile force of a cell was independent of its size or shape. To incorporate the interdependence of cell shape and biochemical signaling, we introduced cell stretch dependent myosin activation into our vertex model to examine motion of cells on ring geometries. This model with signaling also shows coherent angular motion as well as vortex formation as seen in Fig. 3.10 A, and B. This vortex propagates in space and time around the ring as shown in Fig. 3.11.

We also looked at the distribution of mean myosin content and average cell perimeter as a function of radius (shown in Fig. 3.10 C and D). The mean myosin content at the edges of ring seems to be about 20% higher than the myosin content in interior. This is consistent with the cell perimeter distribution in the ring.

3.4 Improvements to the vertex model: Incorporating cell polarization

Persistent force in our model has been defined phenomenologically. In reality, proteins belonging to the Rho family of GTPases Rac, CdC42, and RhoA together determine the direction of motion of the cell. It is known that Rac is essential for lamellipodia protrusion and hence affects persistent motion of the cell.[109,110] It would be interesting to see how the spatial distribution of Rac affects cell shape and if coupling between mechanics and this distribution leads to some emergent properties of collective cell motility.

In our model, we could design the tendency of cell protrusion at a vertex to be

dependent on the local concentration of RacGTPase. Following paragraph describes how this feature could be implemented. Equations for Rac are based on the simple model described in previous single cell modeling studies.[111,112]

PDEs for spatial distribution of GTPases within each cell

A cell is decomposed into finite volumes which are triangles connecting each edge to the center as shown in Fig. 3.13. Each of these volume elements has GTPase in two forms, active G_a and inactive G_{in}. There could be GTPase flux from one volume to the other within the cell but there is none across the cell boundary (reflective boundary conditions at the cell edges). Spatial distribution can be calculated from reaction diffusion equations as shown in Eq. 3.29.

$$\frac{\partial G_a}{\partial t} = D_a \nabla^2 G_a - \nabla \cdot (G_a v) + \left(k_o + \frac{\gamma G_a^2}{k^2 + G_a^2} \right) G_{in} - \delta G_a \tag{3.29}$$

$$\frac{\partial G_{in}}{\partial t} = D_{in} \nabla^2 G_{in} - \nabla \cdot (G_{in} v) - \left(k_o + \frac{\gamma G_a^2}{k^2 + G_a^2} \right) G_{in} + \delta G_a \tag{3.30}$$

Here D_a and D_{in} are diffusion constants for the active and inactive forms of GTPase respectively. There are two reaction terms - one for production and the other for degradation for each form of GTPase. Consider the equation for active GTPase (Eq. 3.29. To integrate this equation over each volume element, the term on the left hand side can be written as

$$\int \frac{\partial G_a}{\partial t} dA = \int \frac{\partial (G_a dA)}{\partial t} - \int \nabla \cdot (G_a v_u) dA \tag{3.31}$$

where v_u is the velocity of the cytoplasm which can be assumed to be equal to the velocity of the cell boundary.[112] Eq. (3.4) now becomes

$$\frac{\partial G_a dA}{\partial t} = \int D_a \nabla^2 G_a dA - \int \nabla \cdot (G_a(v - v_u)) dA + \left(\left(k_o + \frac{\gamma G_a^2}{k^2 + G_a^2} \right) G_{in} - \delta G_a \right) A \quad (3.32)$$

Discretizing the left hand side, the convection term and the reaction term:

$$\begin{aligned} \frac{A^{i+1} G_a^{i+1} - A^i G_a^i}{\Delta t} = \int D_a \nabla^2 G_a dA - \oint \left(G_a^i (v_x^i - v_{ux}^i) \right) n_x + G_a^i (v_y^i - v_{uy}^i) n_y) ds \\ + ((k_o + \frac{\gamma G_a^2}{k^2 + G_a^2}) G_{in} - \delta G_a) A^i \end{aligned} \quad (3.33)$$

The superscript i in the equations represents the time point. The diffusion operator can be discretized as shown in Fig. 3.14. Define

$$q = \nabla G_a \quad (3.34)$$

$$\int_{PT_{i,a}} q \, dA = \int_{PT_{i,a}} \nabla G_a \, dA = \int_{\partial PT_{i,a}} G_a \mathbf{n} \, ds \quad (3.35)$$

$$(3.36)$$

Now the flux through the finite volume can be written as

$$\int D_a \nabla^2 G_a \, dA = \int D_a \, div\colon \mathbf{q} \, dA = \oint \mathbf{q} \cdot \mathbf{n} ds = \sum_{j=1}^{j=3} \mathbf{q} \cdot \mathbf{n}_j \quad (3.37)$$

We then use interpolation to find GTPase values at each vertex. Value at each vertex and the center is chosen to be a weighted sum of all the nearest neighboring finite

volume element values.

$$G_v = \sum_{j=1}^{n} \lambda_j G_j \tag{3.38}$$

such that

$$\sum \lambda_j = 1 \quad \text{if} \quad \lambda_j \geq 0 \tag{3.39}$$

$$\tag{3.40}$$

Similar equations can be written for the inactive form of GTPase.

We assume zero flux across cell boundaries. Hence the net G concentration inside the cell remains the same and there is only conversion between the active and inactive forms such that

$$\sum_{cell} G_a^i + G_{in}^i = 1 \tag{3.41}$$

The protrusive force can now be defined as the vector sum of Rac concentration weighted normal vectors at a vertex. This is illustrated in Fig.3.15 A.

$$F_{p_i} = k_{rac}[G_a \mathbf{n_{l_i}} + G_a \mathbf{n_{r_i}}] \tag{3.42}$$

Assuming that the tendency of a cell to move in a particular direction is proportional to the GTPase concentration, the polarization vector is defined as vector sum of concentrations

multiplied by the outward normal vector of all the finite volumes as shown in Fig. (3.15 B).

$$\mathbf{P} = \sum_{j=1}^{j=n_v} G_j \mathbf{n_j} \tag{3.43}$$

The active form of GTPase is mostly membrane bound and the inactive GTPase form is mostly in the cytosol. Hence the diffusion constant D_a can be assumed to be much less compared to D_{in} and we can further simplify the model by ignoring the diffusion term for active GTPase.

To check this method, we plotted the concentrations of active and inactive GTPases in each cell and correlations in velocity and polarization in the monolayer using this model. The correlations and the preservation of sum of GTPases at 1 shows that the numerical method is stable. This can be seen in Fig. (3.16).

3.5 Discussion

In this chapter, we introduced a vertex based model to study the effects of biochemical signaling on collective cell behavior. This model can potentially be used for studying cells on a variety of substrate geometries. Using this model, we looked at the density dependence of collective cell behavior in terms of mean migration speed. We explored the effects of cell-cell adhesion, friction and contractility on cell motility at various densities. Quantification of mean myosin levels at various densities in experiments validated our stretch dependent myosin activation in the model.

Geometric confinement of cells to rings lead to collective cell rotation with the formation of propagating vortices over different regimes of contractility and persistent force parameters.

We also showed a method to incorporate spatial distribution of signaling proteins using this model. Future work includes incorporating other cellular events such as cell delamination, cell division, rosette formation through vertex transformations. Although it could be computationally expensive, we can potentially build a three dimensional model to explain out of plane events during morphogenesis and also include the effects of curvature of tissue on cell motility.

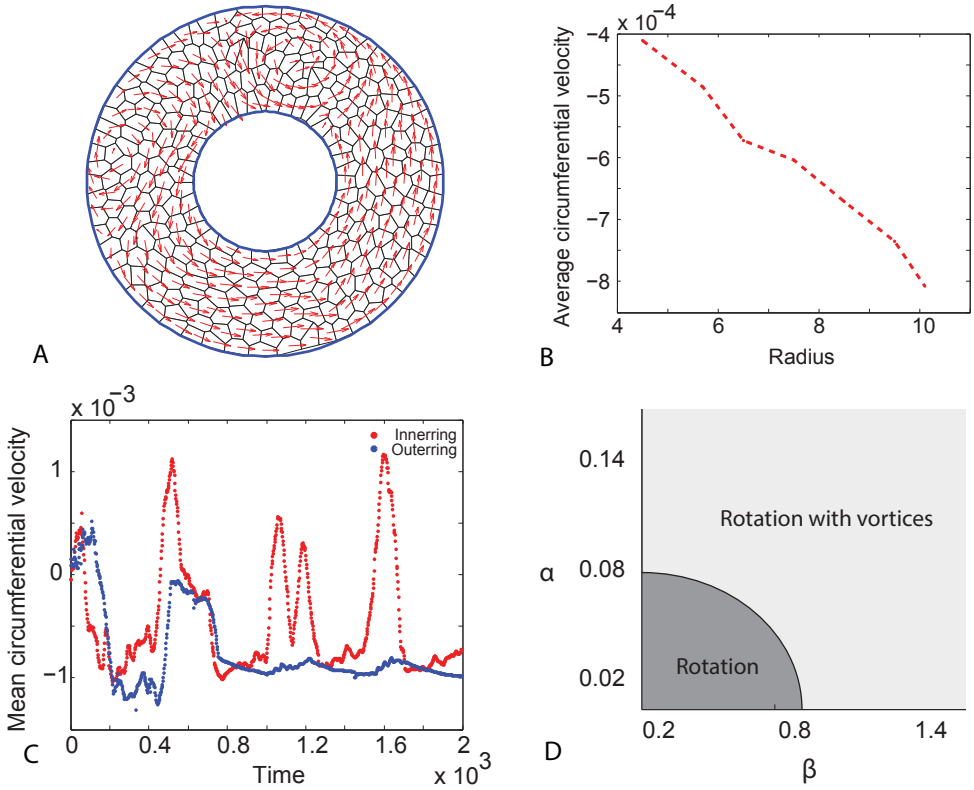

Figure 3.9: Vortex formation in cells on ring substrates. (A) Figure showing rotation with vortices on a ring. (B) Plot showing the average circumferential velocity as a function of ring radius. Positive velocity implies clockwise direction and negative velocity implies counter clockwise direction. Mean circumferential velocity is higher at the outer ring when compared to the inner ring. This is expected in coherent rotation when all the cells move together as a solid body with a constant angular velocity. (C) Plot showing the average circumferential velocity as a function of time. Red circles indicate mean velocity at the inner boundary and blue circles indicate mean velocity at the outer boundary. Mean velocity at the inner boundary shows positive jumps showing clock wise rotation when the velocity at the outer boundary is in the counter clock wise direction. This is indicative of vortex formation as seen in the vortex in (A) where the cells at the inner ring are moving in a direction opposite to the cells at the outer ring. (D) Phase space of persistent force parameters α and β showing the range of parameters in which vortex formation is seen.

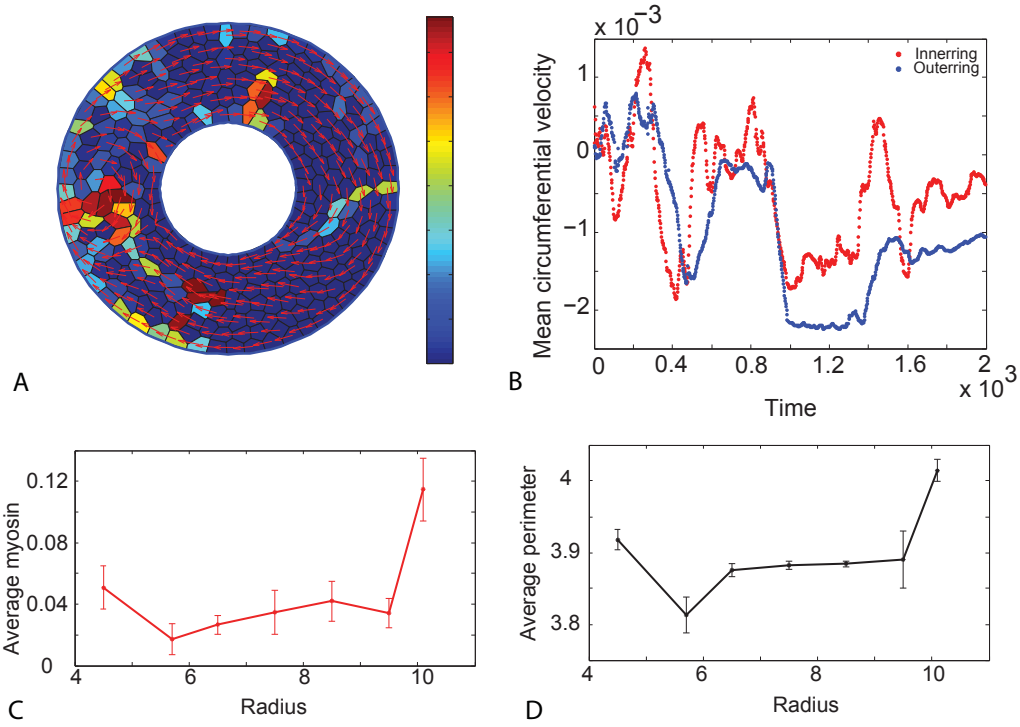

Figure 3.10: Vortex formation and myosin distribution in cells on ring substrates. (A) Figure showing rotation with vortices on a ring using model with signaling. Velocity vectors are shown in red. The cell colors represent activated myosin content; blue to red showing low to high values. (B) Plot showing the average circumferential velocity as a function of time. Red circles indicate mean velocity at the inner boundary and blue circles indicate mean velocity at the outer boundary. Mean velocity at the inner boundary shows positive jumps showing clock wise rotation when the velocity at the outer boundary is in the counter clock wise direction. This is indicative of vortex formation as seen in the vortex in (A) where the cells at the inner ring are moving in a direction opposite to the cells at the outer ring.(C) Plot showing the average myosin content as a function of ring radius. Higher myosin content in the outer ring cells when compared to the inner ring cells. This trend is also reflected in the plot (D) showing average perimeter as a function of radius.

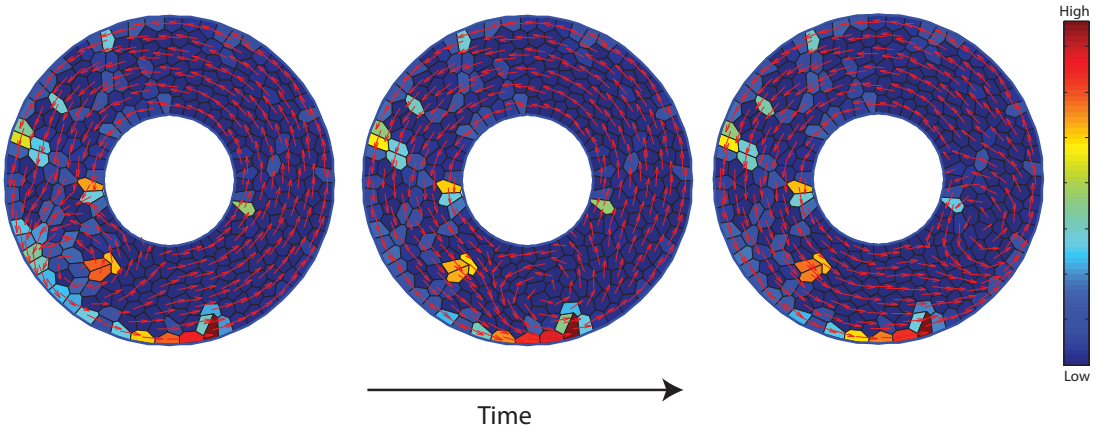

Figure 3.11: Vortex propagation seen.

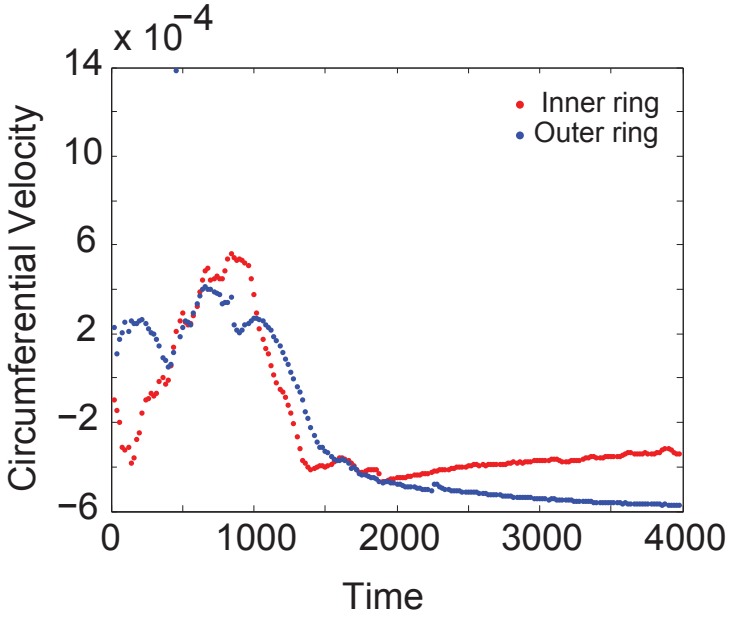

Figure 3.12: Cell velocity at the inner and outer ring boundaries without signaling. Mean circumferential velocity ($n = 4$, $N = 300$)at the inner (red) and outer (blue) boundaries plotted as function of time. Positive velocities represent counter clock wise rotation and negative velocities represent clockwise rotation. Counter rotation at the ring boundaries is not seen.

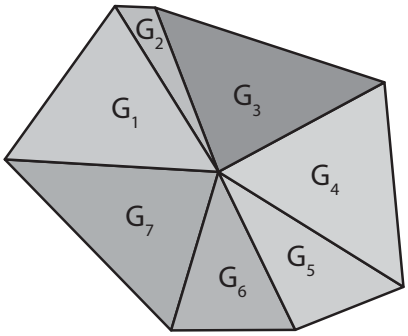

Figure 3.13: Model for spatial distribution of Rac. A cell is decomposed into finite volumes which are triangles connecting each edge to the center.

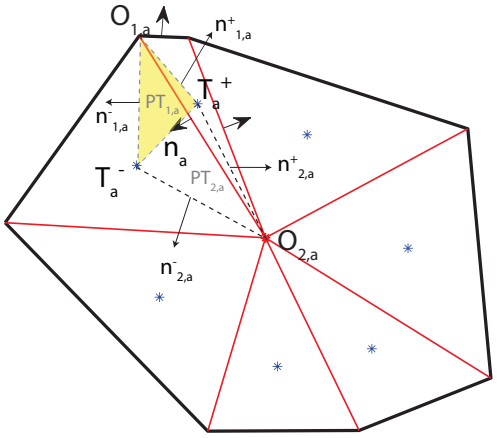

Figure 3.14: Discretizing diffusion operator. Non linear finite volume scheme for diffusion operators

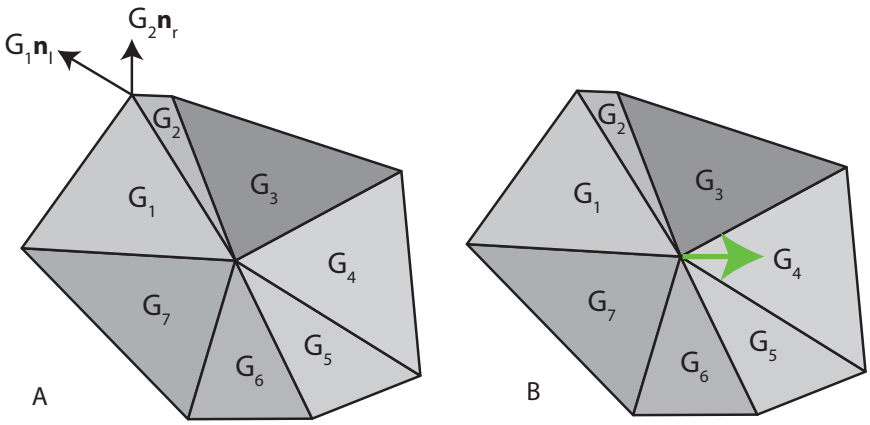

Figure 3.15: Definition of protrusive force and polarization. (A) Protrusive force is defined as the vector sum of Rac concentration weighted normal vectors at a vertex. (B) Vector sum of concentrations multiplied by the outward normal vector of all the finite volumes

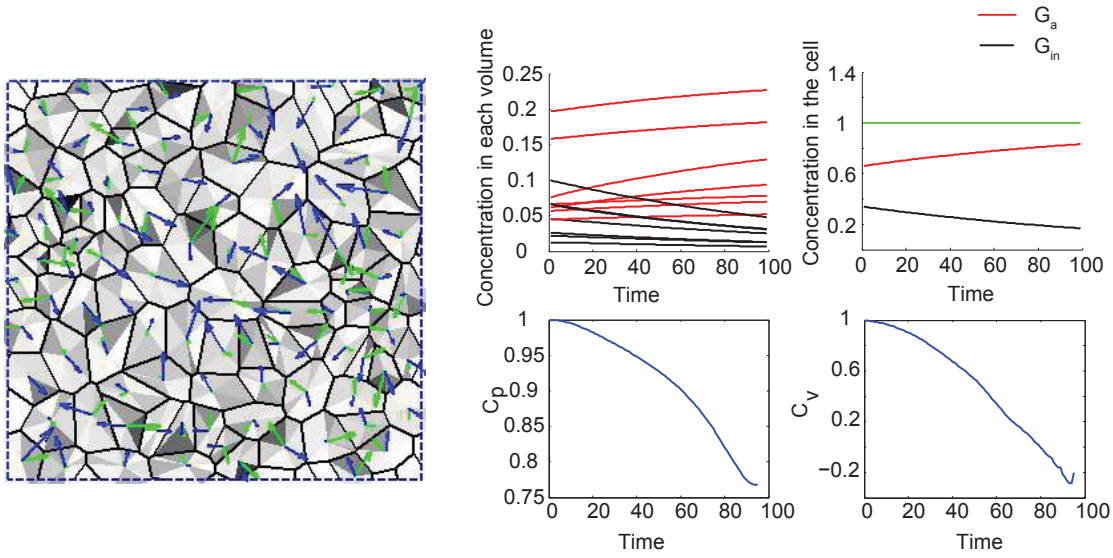

Figure 3.16: Validation of numerical method used. A snapshot of the simulation with spatial distribution of Rac for every cell. The blue vector represents velocity and the green represents polarization. The concenration in the domains for every cell add up to 1.

Chapter 4

A comparison of stochastic simulation methods in mechanobiology

4.1 Introduction

Stochastic simulations are used in biology to understand complex biological phenomena such as movement of molecular motors, quantification of gene expression, and reaction dynamics in a cell. Coupling between mechanics and chemical state change or a conformational change is an important feature of several such biological processes. Molecular motors, transmembrane proteins, ion channels, biopolymers, and adhesion complexes are examples where interplay of mechanics and chemistry plays an crucial role.[113–116]

Such complex systems have many degrees of freedom of which only a few are of

specific interest for analysis. For example, considering a molecular motor, we might be interested only in certain mechanical and chemical states of the protein because they are experimentally observed. These could be length of the protein and whether or not it is bound to ATP.

We can write down the equations of motion for these select degrees of freedom[117] from first principles, assuming the free energy to be a function of these variables and the rest of the variables to be in thermal equilibrium. The free energy of the system as a function of these coordinates could show several local minima separated by barriers and the system could fluctuate between these energetic basins. These fluctuations can be described by time dependent probability distributions.

Considering either continous or discrete probability distributions, stochastic models give us trajectories that jump between basins on an energy landscape.[119] Traditionally, these energy landscapes are approximated to be one dimensional assuming the reaction dynamics along all other coordinates to be much faster and in thermal equilibrium. The reaction is treated as the escape of a brownian particle from a deep energetic basin under the action of a random force according to Kramers theory.[118] This assumption might not hold true when the system has comparable dynamics along one or more coordinates. In the context of mechanobiology, these coordinates could be mechanical and chemical states of a protein. In this chapter, we explore the reaction dynamics in systems where the mechanical and chemical coordinates are on equal footing and are coupled. To do so, we use the simplest form of a two dimensional energy landscape as described below.

4.1.1 Potential energy as a function of mechanical and chemical coordinates

Consider a symmetric potential of the form[120]

$$V(x,s) = U(s) + \frac{1}{2}K(x-s)^2 \tag{4.1}$$

where x represents the mechanical coordinate, s represents the chemical coordinate and K is the coupling constant. $U(s)$ is assumed to be biquadratic in s of the form

$$U(s) = \Delta U(s^2-1)^2 \tag{4.2}$$

where ΔU is the barrier height. This potential can be written in the following form

$$V(x,s) = \Delta U((s^2-1)^2 + 2\tilde{K}(x-s)^2) = \Delta U\tilde{V}(x,s) \tag{4.3}$$

where

$$\tilde{K} = \frac{K}{4\Delta U} \tag{4.4}$$

Contour of the potential as a function of x and s is shown in Fig.1(A). It has two energetic basins, one at $(-1,-1)$ and one at $(1,1)$ and a barrier around the origin between the two wells. Potential as a function of the chemical coordinate along the $x = s$ line is shown in Fig.1(B). For a fixed mechanical coordinate, there are two local minima for the chemical coordinate. For a fixed chemical coordinate, there is one local minimum for the mechanical coordinate.

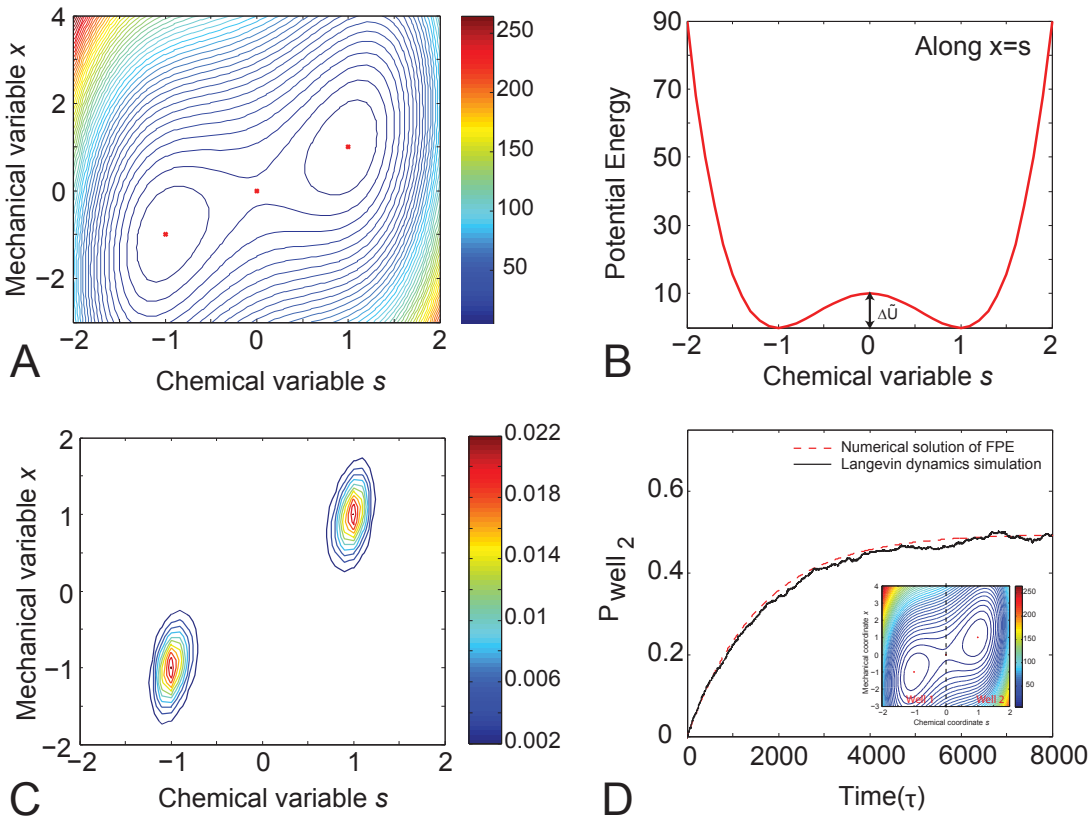

Figure 4.1: Potential energy considered (A) Contour plot of the potential considered as a function of mechanical and chemical variables, x and s respectively. (B) Potential energy profile along $x = s$. $\Delta\tilde{U}$ is the barrier height.(C) Steady state solution of the Fokker Plank Equation, FPE associated with the potential, showing the probability of finding a particle at a certain x and s coordinate at long times. (D) Probability of finding a particle in well 2 (defined as shown in inset) as a function of time obtained from numerical solution of the FPE. This is compared to the probability obtained from Langevin dynamics simulations.

Since inertia is negligible in biological processes, due to very low Reynolds number, the stochastic dynamics of a particle in a potential as in (4.3) can be well described by over

damped Langevin equations along the mechanical and chemical coordinates.

$$\gamma_x \frac{dx}{dt} = -\frac{\partial V(x,s)}{\partial x} + R_x(t) \tag{4.5}$$

$$\gamma_s \frac{ds}{dt} = -\frac{\partial V(x,s)}{\partial s} + R_s(t) \tag{4.6}$$

where $R_x(t), R_s(t)$ are random forces.

4.1.2 Fokker Planck equation to solve for probability *P(x,s,t)*

Instead of analyzing multiple particle trajectories using Langevin equations, it is more convenient to look at the time dependent probability distribution $P(x,s,t)$ representing many trajectories averaged over random forces. The evolution of this probability over the landscape in Eq. 4.3, satisfies the Fokker Planck equation (in the high friction limit) of the form

$$\frac{\partial P}{\partial t} = \underbrace{D_x \frac{\partial^2 P}{\partial x^2} + D_s \frac{\partial^2 P}{\partial s^2}}_{\text{Diffusion}} + \underbrace{\gamma_x \frac{\partial}{\partial x}\left(\frac{\partial V}{\partial x} P\right) + \gamma_x \frac{\partial}{\partial s}\left(\frac{\partial V}{\partial s} P\right)}_{\text{Drift}} \tag{4.7}$$

Here D_x and D_s are the diffusion coefficients and γ_x and γ_s are the frictional drag coefficients along the x and s coordinates respectively. This can be derived from the Langevin equations from first principles.[124]

Non dimensionalizing this equation :

Assuming x and s as dimensionless coordinates, the dimension of D_x is (t^{-1}). Defining

dimensionless parameters

$$\tau = D_x.t \tag{4.8}$$

$$\epsilon = \frac{D_x}{D_s} = \frac{\gamma_s}{\gamma_x} \tag{4.9}$$

$$\Delta\tilde{U} = \frac{\Delta U}{kT} \tag{4.10}$$

Thus, the equation can now be written in the dimensionless form as

$$\frac{\partial P}{\partial \tau} = \left\{ \frac{\partial}{\partial x}\left[\frac{\partial}{\partial x} + \Delta\tilde{U}\frac{\partial \tilde{V}}{\partial x}\right] + \frac{1}{\epsilon}\frac{\partial}{\partial s}\left[\frac{\partial}{\partial s} + \Delta\tilde{U}\frac{\partial \tilde{V}}{\partial s}\right]\right\} P \tag{4.11}$$

Hence $\epsilon, \Delta\tilde{U}$ and $\tilde{K}$ are the three independent dimensionless parameters that define this system.

To compare different simulation methods, the two dimensional x-s space is divided into two regions - one to the left (well 1) and the other to right (well 2) of s=0 line, as shown in Fig. 1(D, inset). Assuming that the particle starts from the point $(-1, -1)$ in well 1, the evolution of probability in region 2 is calculated from the numerical solution of Eq. 4.11 (Details in Appendix S1). This probability of a particle in region 2 as a function of time and the reaction rate are compared with that obtained from different simulation methods described below.

4.2 Simulation Methods

Langevin dynamics (LD) simulations

Non dimensionalization of Langevin equations in x and s dimensions would give equations of the form as shown below in Eq. 4.12 and Eq. 4.13.

$$dx = -\left(\Delta\tilde{U}\frac{\partial\tilde{V}}{\partial x}\bigg|_{\tau} d\tau\right) + r_1\sqrt{2d\tau} \tag{4.12}$$

$$ds = -\left(\frac{1}{\epsilon}\Delta\tilde{U}\frac{\partial\tilde{V}}{\partial s}\bigg|_{\tau} d\tau\right) + r_2\sqrt{\frac{2d\tau}{\epsilon}} \tag{4.13}$$

where the first term on the right hand side in both the equations represents deterministic forcing and the second term represents Brownian force. r_1, r_2 are random numbers taken from a normal distribution with mean zero and standard deviation 1. x and s are propagated according to Eqs. 4.12 and 4.13 in LD simulations.

Fixed time step simulation: x - continuous, s - discrete

In this simulation method, x is a continuous variable but s is discrete; it can be in one of the two states, $s_1 = -1$ or $s_2 = 1$, corresponding to well 1 or well 2 respectively and can undergo Markovian jumps between the two states. For every time step $d\tau$, x is propagated using the Langevin equation (Eq.4.12), assuming the same state of s as at the previous instant of time. This is graphically shown in Fig. 2(A). The position x at the next time step is mathematically expressed as below.

$$x(\tau + d\tau) = x(\tau) + dx \tag{4.14}$$

To find $s(\tau + d\tau)$, the rate of escape from the current state is calculated as follows. The rate of escape from well 1 to well 2 is given by a constant multiplied by a Boltzmann factor of the form

$$k_f = k_o \exp(-\Delta\tilde{U}\Delta\tilde{V}) \tag{4.15}$$

where

$$\Delta\tilde{V} = \tilde{V}(x(\tau), s_2) - \tilde{V}(x(\tau), s_1) \tag{4.16}$$

The rate of escape from well 2 to well 1 is assumed to be a constant

$$k_b = k_o \tag{4.17}$$

The rate constant k_o has to be dimensionless as our time τ is dimensionless. This parameter is usually estimated from experimental data.

If the time taken for escape, i.e, the inverse of the rate is less than the time step $d\tau$, a jump is made along the s coordinate.[121] If not, there is no change in s.

Equilibrium based simulation: Splitting rate expression using λ

In this simulation, the system only jumps from one well to the other. This is graphically shown in Fig. 2(B). In the figure, R represents the bottom of well 1 at $(-1, -1)$ and P represents well 2 at $(1, 1)$. The rates for forward ($R \to P$) and backward($P \to R$) reactions are given as

$$k_f = k_o \exp(-\lambda\Delta\tilde{U}\Delta\tilde{V}) \tag{4.18}$$

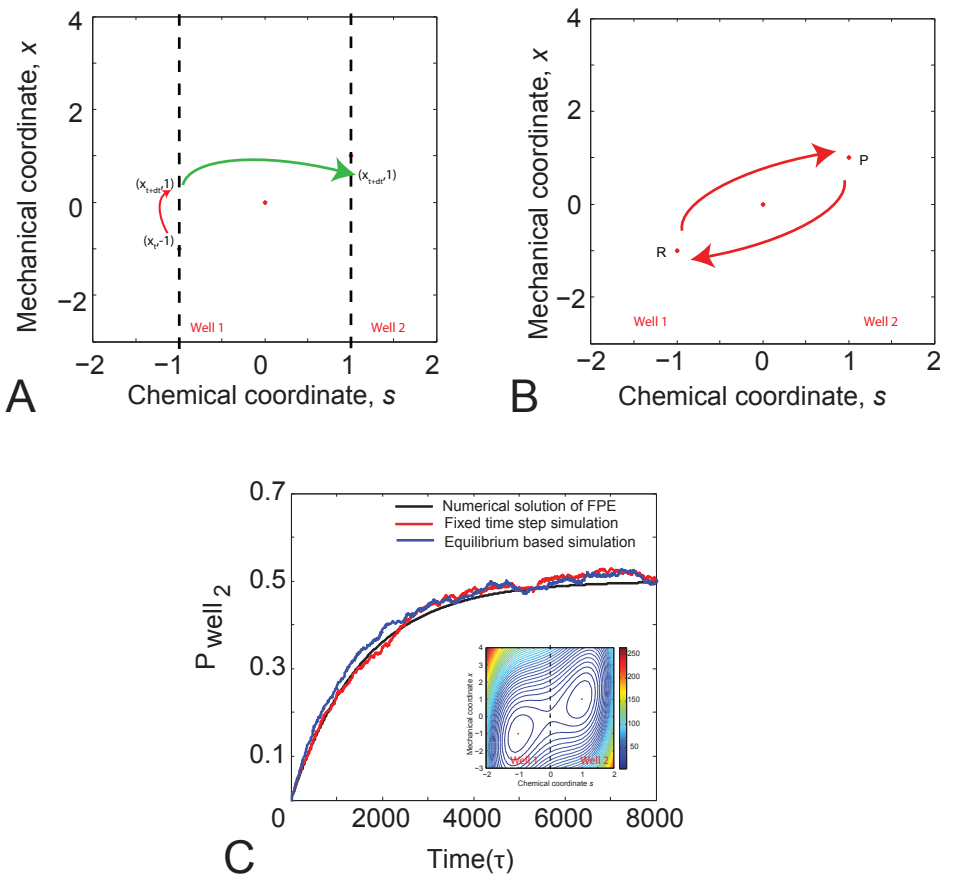

Figure 4.2: Graphical representation of simulation methods used. Broadly, two kinds of simulations are considered in this study - (A)Fixed time step simulations - Here, the x coordinate is propagated using Langevin equation while the s coordinate is discrete and jumps are made between these states. (B)Equilibrium based simulations where the particle jumps from one well to the other. (C)Plot showing the evolution of probability of finding a particle in well 2 as a function of time using equilibrium based and fixed time step simulations.

where

$$\Delta\tilde{V} = \tilde{V}_P - \tilde{V}_R \tag{4.19}$$

and

$$k_b = k_o \exp((1-\lambda)\Delta\tilde{U}\Delta\tilde{V}) \tag{4.20}$$

where

$$\Delta\tilde{V} = \tilde{V}_R - \tilde{V}_P \tag{4.21}$$

In this paper, we consider **Method 1** to be the case with $\lambda = 0.5$ and **Method 2** to be the case with $\lambda = 0$ - i.e the on rate is a constant. Note that, the forms of rate expression chosen always obey detailed balance.

Equilibrium based simulation: Using rate expressions from Langer's theory

In our case, since the potential energy profile is known, we can also get an estimate of rates from Langer's theory which is based on similar ideas as the Kramers rate theory in the one dimensional case.[122]

$$k_f = k_o \exp\left(\frac{-\Delta V_F}{kT}\right) \tag{4.22}$$

and

$$k_f = k_o \exp\left(\frac{-\Delta V_B}{kT}\right) \tag{4.23}$$

Here

$$k_o = \frac{w_o w_b G(\epsilon)}{2\pi kT\epsilon} \tag{4.24}$$

where w_o and w_b are the frequencies at the reactant well and the barrier top respectively,

$$\Delta V_F = V^{sp} - V^r \tag{4.25}$$

$$\Delta V_B = V^{sp} - V^p \tag{4.26}$$

and

$$G(\epsilon) = \frac{\epsilon}{2}\left\{\frac{1}{\epsilon}(1-\tilde{K}) - \tilde{K} + \sqrt{(\frac{1}{\epsilon}(1-\tilde{K}) - \tilde{K})^2 + \frac{4\tilde{K}}{\epsilon}}\right\} \tag{4.27}$$

where V^{sp},V^r and V^p are potentials at saddle point, reactant well and the product well respectively and $G(\epsilon)$ is a function of friction anisotropy $\epsilon = \frac{\gamma_s}{\gamma_x}$ and the coupling constant $\tilde{K}$.

4.3 Results

4.3.1 Validation of numerical solution from FPE by comparison with Langevin dynamics simulations

To obtain the probability of a finding a particle in the x-s space, the non dimensionalized Fokker Planck equation (FPE) as shown in Eq. 4.11 is solved numerically using the Chang Cooper scheme[123] (Details given in SI). The analytical solution of FPE matches the steady state result from the numerical scheme as shown in Fig. 1(C).

To validate the numerical results, a comparison is made between the FPE results and two dimensional Langevin dynamics(LD) simulations. For the same parameter set and initial conditions, the LD simulation is run for 1000 particles for 8000 time steps with each time step corresponding to $d\tau = 0.001$ (dimensionless). The probability of finding a particle in region 2 - defined as the region containing positive s coordinates or region to the right of the $s = 0$ line - is calculated. As shown in Fig. 1 (D), the numerical solution from FPE and the Langevin dynamics simulations are in good agreement.

4.3.2 Comparison of fixed time step and equilibrium based simulation methods

Fixed time step simulations - The mechanical coordinate x is propagated according to the Langevin equation, as shown in Eq. 4.12. At every time step, the time to jump between states along s coordinate is calculated. Only if this time is less than the time step $d\tau$, a jump in s is made. We used a constant off rate and an on rate which depends on potential energy difference between states before and after the jump as shown in Eqs. 4.15 and 4.17. The value used for k_o is 5×10^{-3}.

Equilibrium based simulations - In this method, a particle can only be in one of the two wells and jumps are made between these two states. The rates expressions used are as shown in Eqs. 4.18 and 4.20. The values used for k_o and λ are 3×10^{-4} and 0.5 respectively.

The values of k_o in both these simulations are obtained by fitting the probability curve with the numerical solution from FPE in the standard case with $\epsilon = 1$ and no external force. The same value of k_o is used for all the equilibrium based simulations in the paper.

Comparison between fixed time step and equilibrium simulations - Plots showing the evolution of probability in region 2 as a function of time, using fixed time step simulation and the equilibrium based simulations are shown in Fig. 2(C). The value used for k_o is two orders different in both the simulations. Time taken for the fixed time step simulation is much longer (in the order of hours) compared to the equilibrium simulations (in the order of minutes).

4.3.3 Modifying the potential by introducing a work term $\tilde{F}x$

In the presence of an external force, the potential is modified as follows

$$V(x,s) = \Delta U((s^2-1)^2 + 2\tilde{K}(x-s)^2 - 4\tilde{F}x) \tag{4.28}$$

where

$$\tilde{F} = \left(\frac{F}{4\Delta U}\right) \tag{4.29}$$

The potential energy profiles along the $x = s$ direction with increasing values of $\tilde{F}$ from 0.001-0.25 are shown in Fig.3(A). A comparison of probabilities in region 2 as a function of time is shown for different equilibrium based simulations for one of the values of $\tilde{F}$ in Fig. 3(B). Simulations based on Langer rates and Method 1 are closer to the numerical solution of FPE than simulations based on Method 2. Comparison of rates at various values of $\tilde{F}$ for different simulation methods is shown in Fig. 3 (C,D) for different values of coupling constant, $\tilde{K}$. At lower forces, the simulations based on Langer rates and Method 1 work well and are quite comparable to the FPE solution. At forces higher than 0.1, rates diverge from the true value. Note that the simulations using Langer rates also fail to converge to the rate obtained from solving the FPE.

Clearly, Method 2 does not work well, in the presence of an external force. This implies that the value of k_o cannot be maintained a constant if there is a varying external force on the system, in simulations using Method 2 - where the forward rate is maintained a constant independent of changes in system energy.

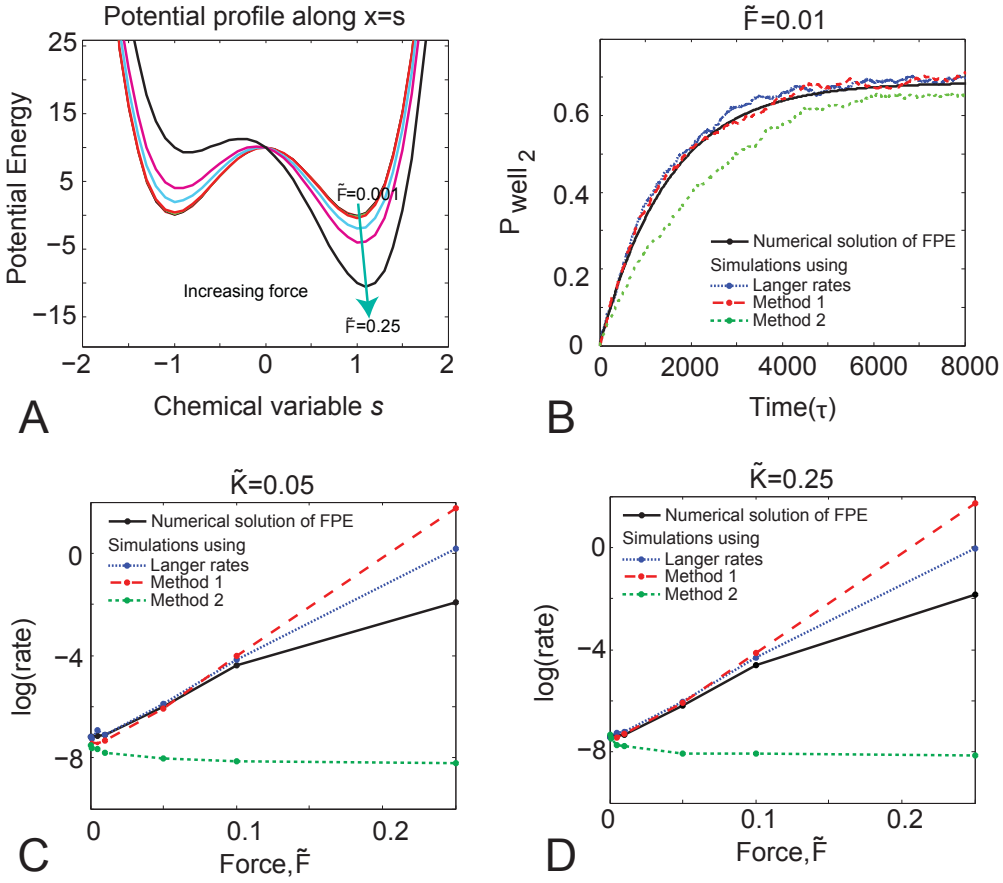

Figure 4.3: Adding an external force. (A) Potential energy profiles along x=s with increasing external force. (B) Probability of finding a particle in well 2 as a function of time, at $\tilde{F}$=0.01 - comparison between the numerical solution of the FPE and simulations using Langer rates and the Methods 1 and 2. (C) Rate constants are calculated by fitting the probability plot to a exponential of the form $a + b\exp(-ct)$. Log of this rate is plotted a function of increasing force $\tilde{F}$ for different coupling constants, $\tilde{K}$=0.05 and (D) $\tilde{K}$=0.25.

4.3.4 Varying friction anisotropy, ϵ

The ratio of diffusion coefficients along the mechanical and the chemical coordinates - $\frac{D_x}{D_s}$ or equivalently the ratio of friction coefficients - $\frac{\gamma_s}{\gamma_x}$ is denoted by ϵ. This

parameter, ϵ is varied such that diffusion along the mechanical coordinate is either 100 or 10 times slower, equal to (which is our standard case) or 10 times faster than the chemical coordinate.

Polar histograms of the angles made by the displacement vectors of particle trajectories in each of these cases is shown in Fig. 4(A). Displacement in the direction of the chemical reaction coordinate is more frequent at low values of ϵ and vice versa for higher values.

Simulation methods are compared while varying ϵ. Here, for Method 1, the rate constant k_o used is scaled by friction anisotropy as follows -

$$k_o(\epsilon) = \frac{k_o}{\epsilon} \tag{4.30}$$

Plotting rates as a function of friction anisotropy (Fig. 4(B)) shows that when diffusion along the mechanical coordinate is comparable or faster than that along the chemical coordinate, simulations using Langer rates or the rate splitting method are in reasonable agreement with the numerical solution. In these cases, rates from simulations using Method 1 are within 1% error of the rates obtained using Langers formula. Errors arise both with Langer rates as well as with Method 1 when mechanical coordinate is slower compared to the chemical coordinate. Similar behavior is observed in the presence of an external force on the system.

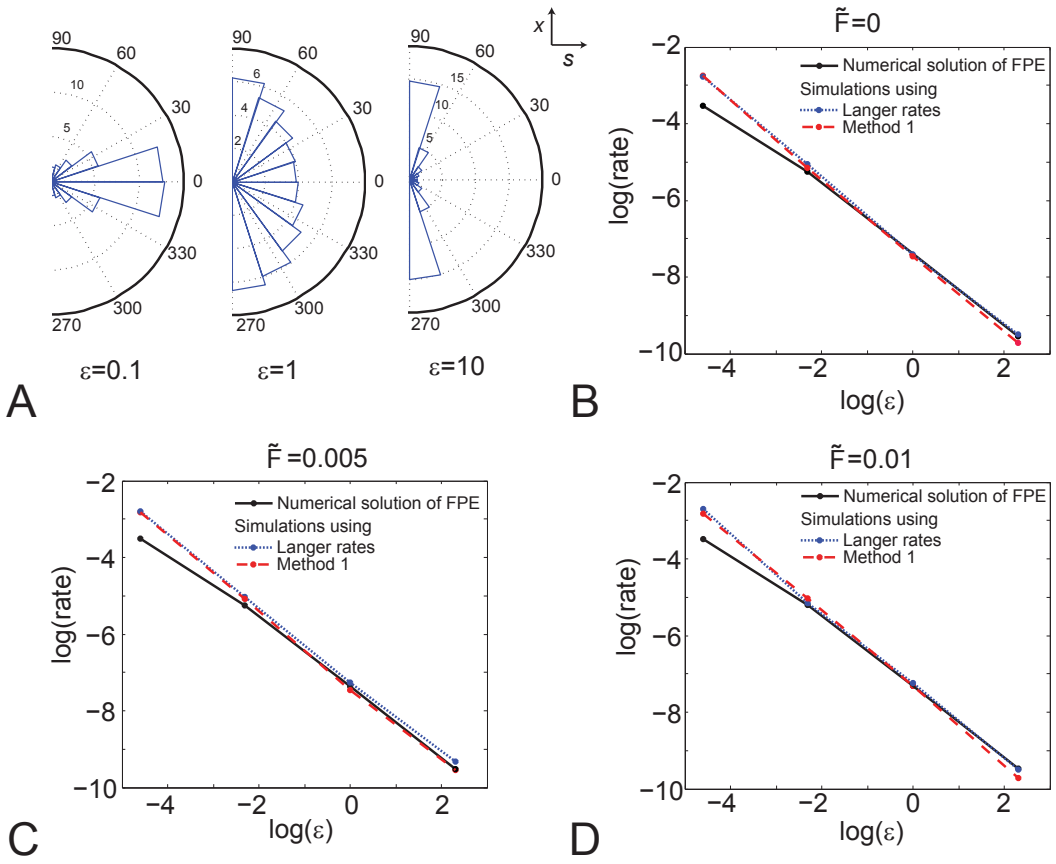

Figure 4.4: Varying friction anisotropy.(A) Polar histograms of angles made by displacement vectors along the trajectory of a particle in a two dimensional potential with different ratios of friction coefficients(ϵ)along the x and s coordinates. (B,C,D) log(rate) plotted as a function of log(ϵ) for different values of external force, $\tilde{F}$.

4.4 Discussion

Through our study we have demonstrated the following. Given a two dimensional energy landscape, fixed time step and equilibrium simulations give reasonably accurate results. We suggest using the equilibrium based simulation as it shows no deviation from the fixed time step method and is much faster.

On and off rates in the model cannot be maintained constants in the presence of an external force on the system. If there is an external force on the system, both rates should include a dependence on force.

When diffusion along the mechanical coordinate is comparable or faster than that along the chemical coordinate, and in the absence or presence of an external force, simulations using Langer rates or the rate splitting method are in reasonable agreement with the numerical solution.

In conclusion, the rate splitting method is a good way of modeling stochastic processes dependent on both mechanical and chemical reaction coordinates with a coupling between them.

Supporting Information

Table 4.1: Parameters used.

$\Delta\tilde{U}$	10	Barrier height (in kT)
$\tilde{K}$	0.01-0.25	Normalized coupling coefficient
ϵ	0.01-10	Ratio of diffusion coefficients
$\tilde{F}$	0.001-0.25	Normalized external force

S1 Numerical scheme - Chang Cooper method

Numerical solution of the Fokker Planck equation in two dimensions To solve Eq. 4.11 numerically, we used the Chang Cooper method.[123] The right hand side of Eq. 4.11 can be written as a derivative of a flux in the x and s directions.

$$\frac{\partial P}{\partial \tau} = \frac{\partial F_x}{\partial x} + \frac{\partial F_s}{\partial s} \tag{4.31}$$

where

$$F_x = \frac{\partial P}{\partial x} + \Delta\tilde{U}\frac{\partial \tilde{V}}{\partial x}P \tag{4.32}$$

$$F_s = \frac{1}{\epsilon}\left(\frac{\partial P}{\partial s} + \Delta\tilde{U}\frac{\partial \tilde{V}}{\partial s}P\right) \tag{4.33}$$

The grid points for the numerical scheme in the x direction are given by i and grid points in the s direction are given by j. Each term on the right side of Eq. 4.31 can be written in a central difference scheme around point (i, j). For instance, in the x direction,

$$\frac{\partial F_x}{\partial x} = \frac{F_{x_{i+\frac{1}{2},j}} - F_{x_{i-\frac{1}{2},j}}}{\Delta x} \tag{4.34}$$

Now, the flux at point $i + \frac{1}{2}$ can be given as

$$F_{x_{i+\frac{1}{2},j}} = \frac{P_{i+1,j} - P_{i,j}}{\Delta x} + \Delta\tilde{U}\frac{\partial \tilde{V}}{\partial x}\bigg|_{i+\frac{1}{2},j} P_{i+\frac{1}{2},j} \tag{4.35}$$

The point $P_{i+\frac{1}{2},j}$ has to lie somewhere between $P_{i,j}$ and $P_{i+1,j}$ along the i direction.

According to the Chang-Cooper scheme, this is given as

$$P_{i+\frac{1}{2},j} = (1-\delta_{i+1})P_{i+1,j} + \delta_{i+1}P_{i,j} \tag{4.36}$$

But we know that at equilibrium, flux has to be equal to zero. Therefore,

$$F_{x_{i+\frac{1}{2}}} = \frac{P_{i+1,j} - Pi,j}{\Delta x} + \Delta\tilde{U}\frac{\partial\tilde{V}}{\partial x}\bigg|_{i+\frac{1}{2},j}((1-\delta_{i+1})P_{i+1,j} + \delta_{i+1}P_{i,j}) = 0 \tag{4.37}$$

From equation [4.37], we can calculate the ratio $\frac{P_{i+1,j}}{P_{i,j}}$ at equilibrium. We know that at equilibrium

$$\frac{P_{i+1,j}}{P_{i,j}} = e^{\Delta\tilde{U}(\tilde{V}(i+1,j)-\tilde{V}(i,j))} \tag{4.38}$$

Let call this ratio K. From equations [4.38] and [4.37], δ_{i+1} can be calculated as

$$\delta_{i+1} = \frac{1}{\Delta\tilde{U}\frac{\partial\tilde{V}}{\partial x}\Big|_{i+\frac{1}{2}}\Delta x} - k_r \tag{4.39}$$

where

$$k_r = \frac{K}{1-K} \tag{4.40}$$

Now, all parts of Eq. 4.35 are known. Similarly $F_{x_{i-\frac{1}{2}}}$ can also be evaluated. A similar procedure in the s direction as well completes the right hand side of equation [4.31]. The time derivative on the left hand side of equation [4.31] is given by a forward difference scheme as

$$\frac{\partial P}{\partial\tau} = \frac{P_{i,j}^{n+1} - P_{i,j}^{n}}{\Delta\tau} \tag{4.41}$$

We have used an implicit Chang Cooper scheme, which implies that all the values on the right hand side of equation [4.31] are at time point $n+1$. Thus, written in the matrix form, the equation would look like

$$P^{n+1} = A^{-1}P^n \tag{4.42}$$

where A is the coefficient matrix. The boundary conditions used are reflective, i.e., the flux is zero across the boundaries. The initial condition used is a dirac delta function at well 1 $(-1,-1)$. The values used for the dimensionless parameters in the numerical method are given in Table [4.1]. Running this simulation for long times gives a steady state solution as shown in Fig. 1(C) which compares well with the analytical solution. The probability as a function of time in well 2 (1,1) is plotted in Fig. 1(D). The width of the well is chosen to be $20\Delta s$ in the s direction and $40\Delta x$ in the x direction. This basically divides the entire domain in half at s=0; each half representing a well.

S2 Nondimensionalization of Langevin equations

Nondimensionalizing Langevin equations in x and s

$$dx = -\frac{1}{\gamma_x}\frac{\partial V}{\partial x}dt + r_1\sqrt{\frac{2kTdt}{\gamma_x}} \tag{4.43}$$

Here,

$$-\frac{1}{\gamma_x}\frac{\partial V}{\partial x}dt = -\frac{1}{\gamma_x}\Delta U\frac{\partial \tilde{V}}{\partial x}\frac{d\tau}{D_x} \tag{4.44}$$

$$= -\Delta\tilde{U}\frac{\partial \tilde{V}}{\partial x}d\tau \tag{4.45}$$

and

$$\sqrt{\frac{2kTdt}{\gamma_x}} = \sqrt{2D_x dt} = \sqrt{2d\tau} \tag{4.46}$$

Similarly

$$ds = -\frac{1}{\gamma_s}\frac{\partial V}{\partial s}dt + r_2\sqrt{\frac{2kTdt}{\gamma_s}} \tag{4.47}$$

Here,

$$-\frac{1}{\gamma_s}\frac{\partial V}{\partial s}dt = -\frac{1}{\gamma_s}\Delta U\frac{\partial \tilde{V}}{\partial s}\frac{d\tau}{\epsilon D_s} \tag{4.48}$$

$$= -\frac{1}{\epsilon}\Delta\tilde{U}\frac{\partial \tilde{V}}{\partial s}d\tau \tag{4.49}$$

and

$$\sqrt{\frac{2kTdt}{\gamma_s}} = \sqrt{2D_s dt} = \sqrt{\frac{2d\tau}{\epsilon}} \tag{4.50}$$

S3 Langer's theory estimate for rate constant in two dimensions

Derivation of rate constant using Langer's theory

$U(s)$ is assumed to be of the following form

$$U(s) = \begin{cases} \frac{1}{2}\omega_o^2(|s|-1)^2 & \text{near the well bottoms } s = 1, -1 \\ \Delta U - \frac{1}{2}\omega_b^2 s^2 & \text{near the barrier top } s = 0 \end{cases} \tag{4.51}$$

Here ω_o represents the well frequency and ω_b is the barrier frequency. These are assumed

as follows

$$\omega_o^2 = 8\Delta U \tag{4.52}$$

$$\omega_b^2 = 4\Delta U \tag{4.53}$$

According to Langer's theory, the rate (T_{2D}) in two dimensions can be approximated as

$$T_{2D} = \frac{1}{2\pi}\left(\frac{\det \hat{V}^R}{|\det \hat{V}^{sp}|}\right)^{\frac{1}{2}} H \exp\left(-\frac{\Delta V_L}{kT}\right) \tag{4.54}$$

where $\hat{V}^R$ and $\hat{V}^{sp}$ are hessian matrices of the potential energy function at coordinates of the reactant well and saddle point respectively and H is a single positive root of the equation

$$det(\gamma H + \hat{V}^{sp}) = 0 \tag{4.55}$$

where γ is friction coefficient tensor. $\gamma = \begin{pmatrix} \gamma_x & 0 \\ 0 & \gamma_s \end{pmatrix}$,

$\hat{V}^R = \begin{pmatrix} K & -K \\ -K & \omega_o^2 + K \end{pmatrix}$ and $\hat{V}^{sp} = \begin{pmatrix} K & -K \\ -K & -\omega_b^2 + K \end{pmatrix}$

On expanding Eq. 4.55,

$$\left(\tilde{\gamma}_s \tilde{H} - 1 + \tilde{K}\right)\left(\tilde{\gamma}_x \tilde{H} + \tilde{K}\right) = \tilde{K}^2 \tag{4.56}$$

where $\tilde{\gamma}_s$, $\tilde{\gamma}_x$, $\tilde{H}$ are $\frac{\gamma_s}{\omega_b}$, $\frac{\gamma_x}{\omega_b}$ and $\frac{H}{\omega_b}$ respectively.

Solving Eq. 4.56 for $\tilde{\gamma_x}$ =0, we get $\tilde{H}(0, \tilde{\gamma}_s) = \frac{1}{\tilde{\gamma}_s}$. Assuming $\tilde{H}(\tilde{\gamma}_x, \tilde{\gamma}_s)$ is of the

form

$$\tilde{H}(\tilde{\gamma}_x, \tilde{\gamma}_s) = \tilde{H}(0, \tilde{\gamma}_s)F(\epsilon) \tag{4.57}$$

ans substituting this in Eq. 4.56, gives

$$F(\epsilon) = \frac{\epsilon}{2}\left\{\frac{1}{\epsilon}(1-\tilde{K}) - \tilde{K} + \sqrt{(\frac{1}{\epsilon}(1-\tilde{K}) - \tilde{K})^2 + \frac{4\tilde{K}}{\epsilon}}\right\} \tag{4.58}$$

Therefore

$$T_{2D} = \frac{\omega_o}{2\pi}\frac{F(\epsilon)}{\tilde{\gamma}_s}\exp\left(\frac{-\Delta V_L}{kT}\right) \tag{4.59}$$

$$T_{2D} = \frac{w_o w_b F(\epsilon)}{2\pi kT\epsilon}\exp\left(\frac{-\Delta V_L}{kT}\right) \tag{4.60}$$

Here

$$\Delta V_L = V^{sp} - V^r \tag{4.61}$$

Bibliography

[1] T. J. Shaw and P. Martin, "Wound repair at a glance" Journal of Cell Science, vol. 122, no. 18, pp. 32093213, 2009.

[2] J. P. Thiery, J. L. Duband, and G. C. Tucker, "Cell Migration in the Vertebrate Embryo: Role of Cell Adhesion and Tissue Environment in Pattern Formation," Annual Review of Cell Biology, vol. 1, no. 1, pp. 91113, 1985.

[3] D. Wirtz, K. Konstantopoulos, and P. C. Searson, "The physics of cancer: the role of physical interactions and mechanical forces in metastasis," Nat Rev Cancer, vol. 11, no. 7, pp. 512522, 2011.

[4] A. J. Ridley, M. A. Schwartz, K. Burridge, R. A. Firtel, M. H. Ginsberg, G. Borisy, J. T. Parsons, and A. R. Horwitz, "Cell Migration: Integrating Signals from Front to Back," Science, vol. 302, no. 5651, pp. 17041709, 2003.

[5] P. Friedl and D. Gilmour, "Collective cell migration in morphogenesis, regeneration and cancer," Nat Rev Mol Cell Biol, vol. 10, no. 7, pp. 445457, 2009.

[6] E. Atilgan, D. Wirtz, and S. X. Sun, "Mechanics and Dynamics of Actin-Driven Thin Membrane Protrusions," Biophysical Journal, vol. 90, no. 1, pp. 6576, 2006.

BIBLIOGRAPHY

[7] K. Burridge and M. Chrzanowska-Wodnicka, "Focal adhesions, contractility, and signaling," Annu. Rev. Cell Dev. Biol., vol. 12, pp. 463518, 1996.

[8] D. Bray, Cell Movements: From Molecules to Motility. Garland Science, 2001.

[9] P. M. Bendix, G. H. Koenderink, D. Cuvelier, Z. Dogic, B. N. Koeleman, W. M. Brieher, C. M. Field, L. Mahadevan, and D. A. Weitz, "A Quantitative Analysis of Contractility in Active Cytoskeletal Protein Networks," Biophys J, vol. 94, no. 8, pp. 31263136, 2008.

[10] S. Yamada, D. Wirtz, and S. C. Kuo, "Mechanics of Living Cells Measured by Laser Tracking Microrheology," Biophysical Journal, vol. 78, no. 4, pp. 17361747, 2000.

[11] W. Xu, R. Mezencev, B. Kim, L. Wang, J. McDonald, and T. Sulchek, "Cell Stiffness Is a Biomarker of the Metastatic Potential of Ovarian Cancer Cells," PLoS One, vol. 7, no. 10, 2012.

[12] S. Suresh, "Nanomedicine: Elastic clues in cancer detection," Nat Nano, vol. 2, no. 12, pp. 748749, 2007.

[13] D. Wirtz, K. Konstantopoulos, and P. C. Searson, "The physics of cancer: the role of physical interactions and mechanical forces in metastasis," Nat Rev Cancer, vol. 11, no. 7, pp. 512522, 2011.

[14] S. Suresh, "Biomechanics and biophysics of cancer cells," Acta Biomater, vol. 3, no. 4, pp. 413438, 2007.

[15] M. Lekka, P. Laidler, D. Gil, J. Lekki, Z. Stachura, and A. Z. Hrynkiewicz, "Elasticity

of normal and cancerous human bladder cells studied by scanning force microscopy," Eur Biophys J, vol. 28, no. 4, pp. 312316, 1999.

[16] T. J. C. Harris and U. Tepass, "Adherens junctions: from molecules to morphogenesis," Nat Rev Mol Cell Biol, vol. 11, no. 7, pp. 502514, 2010.

[17] J. M. Halbleib and W. J. Nelson, "Cadherins in development: cell adhesion, sorting, and tissue morphogenesis," Genes Dev., vol. 20, no. 23, pp. 31993214, 2006.

[18] J.-L. Matre, H. Berthoumieux, S. F. G. Krens, G. Salbreux, F. Jlicher, E. Paluch, and C.-P. Heisenberg, "Adhesion Functions in Cell Sorting by Mechanically Coupling the Cortices of Adhering Cells," Science, vol. 338, no. 6104, pp. 253256, 2012.

[19] R. Farooqui and G. Fenteany, "Multiple rows of cells behind an epithelial wound edge extend cryptic lamellipodia to collectively drive cell-sheet movement," J. Cell. Sci., vol. 118, no. Pt 1, pp. 5163, 2005.

[20] T. Omelchenko, J. M. Vasiliev, I. M. Gelfand, H. H. Feder, and E. M. Bonder, "Rho-dependent formation of epithelial leader cells during wound healing," Proc Natl Acad Sci U S A, vol. 100, no. 19, pp. 1078810793, 2003.

[21] X. Wang, L. He, Y. I. Wu, K. M. Hahn, and D. J. Montell, "Light-mediated activation reveals a key role for Rac in collective guidance of cell movement in vivo," Nat Cell Biol, vol. 12, no. 6, pp. 591597, 2010.

[22] A. J. Ewald, A. Brenot, M. Duong, B. S. Chan, and Z. Werb, "Collective Epithelial Migration and Cell Rearrangements Drive Mammary Branching Morphogenesis," Developmental Cell, vol. 14, no. 4, pp. 570581, 2008.

[23] A. J. Engler, S. Sen, H. L. Sweeney, and D. E. Discher, "Matrix elasticity directs stem cell lineage specification," Cell, vol. 126, no. 4, pp. 677689, Aug. 2006.

[24] O. du Roure, A. Saez, A. Buguin, R. H. Austin, P. Chavrier, P. Siberzan, and B. Ladoux, "Force mapping in epithelial cell migration," PNAS, vol. 102, no. 7, pp. 23902395, 2005.

[25] A. Saez, E. Anon, M. Ghibaudo, O. du Roure, J.-M. Di Meglio, P. Hersen, P. Silberzan, A. Buguin, and B. Ladoux, "Traction forces exerted by epithelial cell sheets," J Phys Condens Matter, vol. 22, no. 19, p. 194119, 2010.

[26] X. Trepat, M. R. Wasserman, T. E. Angelini, E. Millet, D. A. Weitz, J. P. Butler, and J. J. Fredberg, "Physical forces during collective cell migration," Nat Phys, vol. 5, no. 6, pp. 426430, 2009.

[27] A. Brugus, E. Anon, V. Conte, J. H. Veldhuis, M. Gupta, J. Colombelli, J. J. Muoz, G. W. Brodland, B. Ladoux, and X. Trepat, Forces driving epithelial wound healing, Nat Phys, vol. 10, no. 9, pp. 683690, Sep. 2014.

[28] J. D. Scott and T. Pawson, "Cell Signaling in Space and Time: Where Proteins Come Together and When Theyre Apart," Science, vol. 326, no. 5957, pp. 12201224, 2009.

[29] A. S. Menko and D. Boettiger, "Occupation of the extracellular matrix receptor, integrin, is a control point for myogenic differentiation," Cell, vol. 51, no. 1, pp. 5157, 1987.

[30] A. J. Garca, M. D. Vega, and D. Boettiger, "Modulation of Cell Proliferation and

Differentiation through Substrate-dependent Changes in Fibronectin Conformation," Mol Biol Cell, vol. 10, no. 3, pp. 785798, 1999.

[31] C. H. Streuli, N. Bailey, and M. J. Bissell, "Control of mammary epithelial differentiation: basement membrane induces tissue-specific gene expression in the absence of cell-cell interaction and morphological polarity," J. Cell Biol., vol. 115, no. 5, pp. 13831395, 1991.

[32] S. He, C. Liu, X. Li, S. Ma, B. Huo, and B. Ji, "Dissecting Collective Cell Behavior in Polarization and Alignment on Micropatterned Substrates," Biophys. J., vol. 109, no. 3, pp. 489500, 2015.

[33] M. Raftopoulou and A. Hall, "Cell migration: Rho GTPases lead the way," Developmental Biology, vol. 265, no. 1, pp. 2332, 2004.

[34] A. J. Ridley, "Rho GTPases and cell migration," Journal of Cell Science, vol. 114, no. 15, pp. 27132722, 2001.

[35] C. D. Nobes and A. Hall, "Rho GTPases Control Polarity, Protrusion, and Adhesion during Cell Movement," J Cell Biol, vol. 144, no. 6, pp. 12351244, 1999.

[36] A. Hall, "Rho GTPases and the Actin Cytoskeleton," Science, vol. 279, no. 5350, pp. 509514, 1998.

[37] Y. C. Poh, S. Na, F. Chowdhury, M. Ouyang, Y. Wang, and N. Wang, "Rapid Activation of Rac GTPase in Living Cells by Force Is Independent of Src," PLoS ONE, vol. 4, no. 11, p. e7886, 2009.

[38] X. H. Zhao, C. Laschinger, P. Arora, K. Szszi, A. Kapus, and C. A. McCulloch, "Force activates smooth muscle -actin promoter activity through the Rho signaling pathway," J Cell Sci, vol. 120, no. 10, pp. 18011809, 2007.

[39] L. He, X. Wang, H. L. Tang, and D. J. Montell, "Tissue elongation requires oscillating contractions of a basal actomyosin network," Nat Cell Biol, vol. 12, no. 12, pp. 11331142, 2010.

[40] A. T. Winfree, The Geometry of Biological Time. Springer, 2001.

[41] A. Goldbeter, Biochemical Oscillations and Cellular Rhythms: The Molecular Bases of Periodic and Chaotic Behaviour. Cambridge University Press, 1997.

[42] J. E. Ferrell, T. Y.-C. Tsai, and Q. Yang, "Modeling the Cell Cycle: Why Do Certain Circuits Oscillate?," Cell, vol. 144, no. 6, pp. 874885, 2011.

[43] M. Amano, K. Chihara, K. Kimura, Y. Fukata, N. Nakamura, Y. Matsuura, and K. Kaibuchi, "Formation of actin stress fibers and focal adhesions enhanced by Rho-kinase," Science, vol. 275, no. 5304, pp. 13081311, 1997.

[44] S. Pellegrin and H. Mellor, "Actin stress fibres," J Cell Sci, vol. 120, no. 20, pp. 34913499, Oct. 2007.

[45] V. Maruthamuthu, B. Sabass, U. S. Schwarz, and M. L. Gardel, "Cell-ECM traction force modulates endogenous tension at cellcell contacts," PNAS, vol. 108, no. 12, pp. 47084713, 2011.

[46] K. Bhadriraju, M. Yang, S. Alom Ruiz, D. Pirone, J. Tan, and C. S. Chen, "Activation

of ROCK by RhoA is regulated by cell adhesion, shape, and cytoskeletal tension," Experimental Cell Research, vol. 313, no. 16, pp. 36163623, 2007.

[47] A. Jilkine, A. F. M. Mare, and L. Edelstein-Keshet, "Mathematical model for spatial segregation of the Rho-family GTPases based on inhibitory crosstalk," Bull. Math. Biol., vol. 69, no. 6, pp. 19431978, 2007.

[48] R. Kalluri, "Basement membranes: structure, assembly and role in tumour angiogenesis," Nat Rev Cancer, vol. 3, no. 6, pp. 422433, 2003.

[49] S. L. Haigo and D. Bilder, "Global tissue revolutions in a morphogenetic movement controlling elongation," Science, vol. 331, no. 6020, pp. 10711074, 2011.

[50] B. Zhang and Y. Zheng, "Regulation of RhoA GTP Hydrolysis by the GTPase-Activating Proteins p190, p50RhoGAP, Bcr, and 3BP-1" Biochemistry, vol. 37, no. 15, pp. 52495257, 1998.

[51] S. Walcott and S. X. Sun, "A mechanical model of actin stress fiber formation and substrate elasticity sensing in adherent cells," PNAS, vol. 107, no. 17, pp. 77577762, 2010.

[52] G. Civelekoglu-Scholey, A. Wayne Orr, I. Novak, J.-J. Meister, M. A. Schwartz, and A. Mogilner, "Model of coupled transient changes of Rac, Rho, adhesions and stress fibers alignment in endothelial cells responding to shear stress," Journal of Theoretical Biology, vol. 232, no. 4, pp. 569585, 2005.

[53] E. Hannezo, J. Prost, and J.-F. Joanny, "Theory of epithelial sheet morphology in three dimensions," Proc. Natl. Acad. Sci. U.S.A., vol. 111, no. 1, pp. 2732, 2014.

BIBLIOGRAPHY

[54] A. C. Martin, M. Kaschube, and E. F. Wieschaus, "Pulsed contractions of an actin-myosin network drive apical constriction," Nature, vol. 457, no. 7228, pp. 495499, 2009.

[55] T. Lecuit and P.-F. Lenne, "Cell surface mechanics and the control of cell shape, tissue patterns and morphogenesis," Nat Rev Mol Cell Biol, vol. 8, no. 8, pp. 633644, 2007.

[56] J. A. Zallen and E. Wieschaus, "Patterned gene expression directs bipolar planar polarity in Drosophila," Dev. Cell, vol. 6, no. 3, pp. 343355, 2004.

[57] A. C. Martin, M. Gelbart, R. Fernandez-Gonzalez, M. Kaschube, and E. F. Wieschaus, "Integration of contractile forces during tissue invagination," J. Cell Biol., vol. 188, no. 5, pp. 735749, 2010.

[58] [1]C. A. Berg, "Tube Formation in Drosophila Egg Chambers," Tissue Engineering Part A, vol. 14, no. 9, pp. 14791488, 2008.

[59] A. Jacinto, S. Woolner, and P. Martin, "Dynamic Analysis of Dorsal Closure in Drosophila: From Genetics to Cell Biology," Developmental Cell, vol. 3, no. 1, pp. 919, 2002.

[60] C Sommer, C Straehle, U Kothe, FA Hamprecht, "ilastik: Interactive Learning and Segmentation Toolkit. 8th IEEE International Symposium on Biomedical Imaging," 2011.

[61] K. Burridge and K. Wennerberg, "Rho and Rac Take Center Stage," Cell, vol. 116, no. 2, pp. 167179, 2004.

[62] R. J. Buchsbaum, "Rho activation at a glance," J Cell Sci, vol. 120, no. 7, pp. 11491152, 2007.

[63] K. Burridge and R. Doughman, "Front and back by Rho and Rac," Nat Cell Biol, vol. 8, no. 8, pp. 781782, 2006.

[64] G. Forgacs, R. A. Foty, Y. Shafrir, and M. S. Steinberg, "Viscoelastic properties of living embryonic tissues: a quantitative study.," Biophys J, vol. 74, no. 5, pp. 22272234, 1998.

[65] J. Solon, A. Kaya-opur, J. Colombelli, and D. Brunner, "Pulsed Forces Timed by a Ratchet-like Mechanism Drive Directed Tissue Movement during Dorsal Closure," Cell, vol. 137, no. 7, pp. 13311342, 2009.

[66] N. S. Gov, "Traction forces during collective cell motion," HFSP J, vol. 3, no. 4, pp. 223227, 2009.

[67] A. Hurwitz, "On the conditions under which an equation has only roots with negative real parts," Math. Ann., vol. 46, no. 2, pp. 273284, 1895.

[68] C. M. Niessen, "Tight Junctions/Adherens Junctions: Basic Structure and Function," J Invest Dermatol, vol. 127, no. 11, pp. 25252532, 2007.

[69] C. M. Niessen and C. J. Gottardi, "Molecular components of the adherens junction," Biochimica et Biophysica Acta (BBA) - Biomembranes, vol. 1778, no. 3, pp. 562571, 2008.

[70] K. J. Green and C. L. Simpson, "Desmosomes: New Perspectives on a Classic," J Invest Dermatol, vol. 127, no. 11, pp. 24992515, 2007.

[71] A. R. Harris, A. Daeden, and G. T. Charras, "Formation of adherens junctions leads to the emergence of a tissue-level tension in epithelial monolayers," J. Cell. Sci., vol. 127, no. Pt 11, pp. 25072517, 2014.

[72] B. Lubarsky and M. A. Krasnow, "Tube morphogenesis: making and shaping biological tubes," Cell, vol. 112, no. 1, pp. 1928, 2003.

[73] J. B. Wallingford, S. E. Fraser, and R. M. Harland, "Convergent Extension: The Molecular Control of Polarized Cell Movement during Embryonic Development," Developmental Cell, vol. 2, no. 6, pp. 695706, 2002.

[74] M. Leptin, "Gastrulation Movements: the Logic and the Nuts and Bolts," Developmental Cell, vol. 8, no. 3, pp. 305320, 2005.

[75] M. Leptin and B. Grunewald, "Cell shape changes during gastrulation in Drosophila," Development, vol. 110, no. 1, pp. 7384, 1990.

[76] S. R. K. Vedula, A. Ravasio, C. T. Lim, and B. Ladoux, "Collective Cell Migration: A Mechanistic Perspective," Physiology, vol. 28, no. 6, pp. 370379, 2013.

[77] D. P. Kiehart, C. G. Galbraith, K. A. Edwards, W. L. Rickoll, and R. A. Montague, "Multiple forces contribute to cell sheet morphogenesis for dorsal closure in Drosophila," J. Cell Biol., vol. 149, no. 2, pp. 471490, 2000.

[78] C. Bertet, L. Sulak, and T. Lecuit, "Myosin-dependent junction remodelling controls

planar cell intercalation and axis elongation," Nature, vol. 429, no. 6992, pp. 667671, 2004.

[79] J. C. Arciero, Q. Mi, M. F. Branca, D. J. Hackam, and D. Swigon, "Continuum model of collective cell migration in wound healing and colony expansion," Biophys. J., vol. 100, no. 3, pp. 535543, 2011.

[80] G. W. Brodland, "Computational modeling of cell sorting, tissue engulfment, and related phenomena: A review," Appl. Mech. Rev, vol. 57, no. 1, pp. 4776, 2004.

[81] G. W. Brodland, D. Viens, and J. H. Veldhuis, "A new cell-based FE model for the mechanics of embryonic epithelia," Comput Methods Biomech Biomed Engin, vol. 10, no. 2, pp. 121128, 2007.

[82] B. Li and S. X. Sun, "Coherent Motions in Confluent Cell Monolayer Sheets," Biophysical Journal, vol. 107, no. 7, pp. 15321541, 2014.

[83] N. Seplveda, L. Petitjean, O. Cochet, E. Grasland-Mongrain, P. Silberzan, and V. Hakim, "Collective Cell Motion in an Epithelial Sheet Can Be Quantitatively Described by a Stochastic Interacting Particle Model," PLoS Comput Biol, vol. 9, no. 3, p. e1002944, 2013.

[84] A. G. Fletcher, M. Osterfield, R. E. Baker, and S. Y. Shvartsman, "Vertex Models of Epithelial Morphogenesis," Biophysical Journal, vol. 106, no. 11, pp. 22912304, 2014.

[85] T. Okuzono and K. Kawasaki, "Intermittent flow behavior of random foams: A computer experiment on foam rheology," Phys. Rev. E, vol. 51, no. 2, pp. 12461253, 1995.

[86] K. Kawasaki, T. Nagai, and K. Nakashima, "Vertex models for two-dimensional grain growth," Philosophical Magazine Part B, vol. 60, no. 3, pp. 399421, 1989.

[87] M. Marder, "Soap-bubble growth," Phys. Rev. A, vol. 36, no. 1, pp. 438440, 1987.

[88] H. Honda and G. Eguchi, "How much does the cell boundary contract in a monolayered cell sheet?," Journal of Theoretical Biology, vol. 84, no. 3, pp. 575588, 1980.

[89] H. Honda, "Description of cellular patterns by Dirichlet domains: The two-dimensional case," Journal of Theoretical Biology, vol. 72, no. 3, pp. 523543, 1978.

[90] T. Nagai and H. Honda, "A dynamic cell model for the formation of epithelial tissues," Philosophical Magazine Part B, vol. 81, no. 7, pp. 699719, 2001.

[91] R. Farhadifar, J.-C. Rper, B. Aigouy, S. Eaton, and F. Jlicher, "The Influence of Cell Mechanics, Cell-Cell Interactions, and Proliferation on Epithelial Packing," Current Biology, vol. 17, no. 24, pp. 20952104, 2007.

[92] G. W. Brodland, V. Conte, P. G. Cranston, J. Veldhuis, S. Narasimhan, M. S. Hutson, A. Jacinto, F. Ulrich, B. Baum, and M. Miodownik, "Video force microscopy reveals the mechanics of ventral furrow invagination in Drosophila," PNAS, vol. 107, no. 51, pp. 2211122116, 2010.

[93] B. M. Burkel, H. A. Benink, E. M. Vaughan, G. von Dassow, and W. M. Bement, "A Rho GTPase signal treadmill backs a contractile array," Dev. Cell, vol. 23, no. 2, pp. 384396, 2012.

[94] C. M. Simon, E. M. Vaughan, W. M. Bement, and L. Edelstein-Keshet, "Pattern

formation of Rho GTPases in single cell wound healing," Mol Biol Cell, vol. 24, no. 3, pp. 421432, 2013.

[95] H. Jiang and S. X. Sun, Cellular Pressure and Volume Regulation and Implications for Cell Mechanics, Biophysical Journal, vol. 105, no. 3, pp. 609619, 2013.

[96] C. W. Wolgemuth and M. Zajac, "The Moving Boundary Node Method: A level set-based, finite volume algorithm with applications to cell motility," J Comput Phys, vol. 229, no. 19, pp. 72877308, 2010.

[97] T. E. Angelini, E. Hannezo, X. Trepat, J. J. Fredberg, and D. A. Weitz, "Cell Migration Driven by Cooperative Substrate Deformation Patterns," Phys. Rev. Lett., vol. 104, no. 16, p. 168104, 2010.

[98] M. Sadati, A. Nourhani, J. J. Fredberg, and N. Taheri Qazvini, "Glass-like dynamics in the cell and in cellular collectives," WIREs Syst Biol Med, vol. 6, no. 2, pp. 137149, 2014.

[99] M. Sadati, N. Taheri Qazvini, R. Krishnan, C. Y. Park, and J. J. Fredberg, "Collective migration and cell jamming," Differentiation, vol. 86, no. 3, pp. 121125, 2013.

[100] K. D. Nnetu, M. Knorr, S. Pawlizak, T. Fuhs, and J. A. Ks, "Slow and anomalous dynamics of an MCF-10A epithelial cell monolayer," Soft Matter, vol. 9, no. 39, pp. 93359341, 2013.

[101] A. Nagafuchi, S. Ishihara, and S. Tsukita, "The roles of catenins in the cadherin-mediated cell adhesion: functional analysis of E-cadherin-alpha catenin fusion molecules," J. Cell Biol., vol. 127, no. 1, pp. 235245, 1994.

BIBLIOGRAPHY

[102] E. M. Balzer, Z. Tong, C. D. Paul, W.-C. Hung, K. M. Stroka, A. E. Boggs, S. S. Martin, and K. Konstantopoulos, "Physical confinement alters tumor cell adhesion and migration phenotypes," FASEB J, vol. 26, no. 10, pp. 40454056, 2012.

[103] S. Huang, C. P. Brangwynne, K. K. Parker, and D. E. Ingber, "Symmetry-breaking in mammalian cell cohort migration during tissue pattern formation: role of random-walk persistence," Cell Motil. Cytoskeleton, vol. 61, no. 4, pp. 201213, 2005.

[104] K. Doxzen, S. R. K. Vedula, M. C. Leong, H. Hirata, N. S. Gov, A. J. Kabla, B. Ladoux, and C. T. Lim, "Guidance of collective cell migration by substrate geometry," Integr. Biol., vol. 5, no. 8, pp. 10261035, 2013.

[105] K. Tanner, H. Mori, R. Mroue, A. Bruni-Cardoso, and M. J. Bissell, "Coherent angular motion in the establishment of multicellular architecture of glandular tissues," PNAS, vol. 109, no. 6, pp. 19731978, 2012.

[106] L. Q. Wan, K. Ronaldson, M. Park, G. Taylor, Y. Zhang, J. M. Gimble, and G. Vunjak-Novakovic, "Micropatterned mammalian cells exhibit phenotype-specific left-right asymmetry," PNAS, vol. 108, no. 30, pp. 1229512300, 2011.

[107] S. R. K. Vedula, M. C. Leong, T. L. Lai, P. Hersen, A. J. Kabla, C. T. Lim, and B. Ladoux, "Emerging modes of collective cell migration induced by geometrical constraints," PNAS, vol. 109, no. 32, pp. 1297412979, 2012.

[108] A.-K. Marel, M. Zorn, C. Klingner, R. Wedlich-Sldner, E. Frey, and J. O. Rdler, "Flow and Diffusion in Channel-Guided Cell Migration," Biophys J, vol. 107, no. 5, pp. 10541064, 2014.

[109] O. Pertz, "Spatio-temporal Rho GTPase signaling - where are we now?," J. Cell. Sci., vol. 123, no. Pt 11, pp. 18411850, 2010.

[110] M. Machacek, L. Hodgson, C. Welch, H. Elliott, O. Pertz, P. Nalbant, A. Abell, G. L. Johnson, K. M. Hahn, and G. Danuser, "Coordination of Rho GTPase activities during cell protrusion," Nature, vol. 461, no. 7260, pp. 99103, 2009.

[111] Y. Mori, A. Jilkine, and L. Edelstein-Keshet, "Wave-Pinning and Cell Polarity from a Bistable Reaction-Diffusion System," Biophysical Journal, vol. 94, no. 9, pp. 36843697, 2008.

[112] C. W. Wolgemuth, J. Stajic, and A. Mogilner, "Redundant Mechanisms for Stable Cell Locomotion Revealed by Minimal Models," Biophys J, vol. 101, no. 3, pp. 545553, 2011.

[113] J. Howard, "Mechanics of Motor Proteins and the Cytoskeleton". Sinauer Associates, Publishers, 2001.

[114] M. Schliwa and G. Woehlke, "Molecular motors," Nature, vol. 422, no. 6933, pp. 759765, 2003.

[115] P. J. Bond and M. S. P. Sansom, "The simulation approach to bacterial outer membrane proteins," Mol. Membr. Biol., vol. 21, no. 3, pp. 151161, 2004.

[116] D. Riveline, E. Zamir, N. Q. Balaban, U. S. Schwarz, T. Ishizaki, S. Narumiya, Z. Kam, B. Geiger, and A. D. Bershadsky, "Focal Contacts as Mechanosensors Externally Applied Local Mechanical Force Induces Growth of Focal Contacts by an

Mdia1-Dependent and Rock-Independent Mechanism," J Cell Biol, vol. 153, no. 6, pp. 11751186, 2001.

[117] P. Hnggi, P. Talkner, and M. Borkovec, "Reaction-rate theory: fifty years after Kramers," Rev. Mod. Phys., vol. 62, no. 2, pp. 251341, 1990.

[118] H. A. Kramers, "Brownian motion in a field of force and the diffusion model of chemical reactions," Physica, vol. 7, no. 4, pp. 284304, 1940.

[119] S. X. Sun, G. Lan, and E. Atilgan, "Chapter 23: Stochastic modeling methods in cell biology," Methods Cell Biol., vol. 89, pp. 601621, 2008.

[120] A. M. Berezhkovskii, V. Y. Zitserman, and A. Polimeno, "Numerical test of Kramers reaction rate theory in two dimensions," The Journal of Chemical Physics, vol. 105, no. 15, pp. 63426357, 1996.

[121] J. S. Kim, C. H. Lee, and P. A. Coulombe, "Modeling the Self-Organization Property of Keratin Intermediate Filaments," Biophys J, vol. 99, no. 9, pp. 27482756, 2010.

[122] J. S. Langer, "Statistical theory of the decay of metastable states," Annals of Physics, vol. 54, no. 2, pp. 258275, 1969.

[123] J. S. Chang and G. Cooper, "A practical difference scheme for Fokker-Planck equations," Journal of Computational Physics, vol. 6, no. 1, pp. 116, 1970.

[124] H. Risken, "The Fokker-Planck Equation", vol. 18. Springer Berlin Heidelberg, 1984.

Vita

Sarita Koride received the Bachelors of Technology degree in Biotechnology from Indian Institute of Technology (IIT), Guwahati in 2010 and entered the Chemical and Biomolecular Engineering Ph.D. program at Johns Hopkins University the same year. She was an institute merit scholar in 2009 - awarded to the the top performing student in every year at IIT. Her doctoral research focuses on understanding cell motility at the tissue level as well as at the cell level through mechanochemical modeling.